TWO-WEEK LOAN COPY

This is a Library Circulating Copy which may be borrowed for two weeks. For a personal retention copy, call Tech. Info. Division, Ext. 5545

DISCLAIMER

This document was prepared as an account of work sponsored by the United States Government. While this document is believed to contain correct information, neither the United States Government nor any agency thereof, nor the Regents of the University of California, nor any of their employees, makes any warranty, express or implied, or assumes any legal responsibility for the accuracy, completeness, or usefulness of any information, apparatus, product, or process disclosed, or represents that its use would not infringe privately owned rights. Reference herein to any specific commercial product, process, or service by its trade name, trademark, manufacturer, or otherwise, does not necessarily constitute or imply its endorsement, recommendation, or favoring by the United States Government or any agency thereof, or the Regents of the University of California. The views and opinions of authors expressed herein do not necessarily state or reflect those of the United States Government or any agency thereof or the Regents of the University of California.

UCRL-11537

UNIVERSITY OF CALIFORNIA
Lawrence Radiation Laboratory
Berkeley, California

AEC Contract No. W-7405-eng-48

SCATTERING OF 250-MeV POSITIVE PIONS BY PROTONS: EXPERIMENT AND ANALYSIS

Wladyslaw Kilian Troka

(Ph. D. Thesis)

September 18, 1964

SCATTERING OF 250-MeV POSITIVE PIONS BY PROTONS: EXPERIMENT AND ANALYSIS

Contents

Abstract v

I. Introduction 1

II. Pion Beam

A. External Proton Beam 5

B. Production of Pions 5

C. Beam Spectrograph 7

D. Pion Beam Characteristics at the Hydrogen Target. 8

III. Differential Cross-Section Measurement

A. Experimental Apparatus 13

1. Counters 13

2. Hydrogen Target 18

3. Electronics 20

B. Experimental Method 23

1. Cerenkov Efficiencies 23

2. Scattering Data 25

IV. Data Reduction

A. Multiple Nuclear-Scattering Corrections 31

1. Hydrogen-Hydrogen 31

2. Hydrogen-Target Walls 35

3. Hydrogen-Counter Materials 40

B. Pion-Decay Correction..... 43

C. Cerenkov-Efficiency Corrections..... 50

1. Efficiency for All Mesons..... 50

2. Fraction of Protons Counted by the Cerenkov. 60

D. Geometrical Correction..... 60

E. Normalization and Results..... 62

F. Errors..... 65

V. Phase-Shift Analysis..... 73

A. Search Program..... 73

1. Scattering Amplitudes..... 73

2. Computing Method..... 76

B. Results..... 82

1. SPD Analysis..... 82

2. SPDF Analysis..... 82

C. Discussion..... 84

Acknowledgments..... 87

Appendices

A. Generalized Cerenkov Efficiency for All Mesons.. 88

B. Coulomb-Corrected Scattering Amplitudes..... 89

C. Tables of Error Matrices for SPD and SPDF Solutions..... 93

References..... 94

SCATTERING OF 250-MeV POSITIVE PIONS BY PROTONS: EXPERIMENT AND ANALYSIS

Wladyslaw Kilian Troka

Lawrence Radiation Laboratory
University of California
Berkeley, California

September 18, 1964

ABSTRACT

The differential cross section for elastic scattering of positive pions on protons has been measured at a nominal incident-meson kinetic energy of 250 MeV. The angular range covered in the center of mass by the 13 data points was 14.9 deg to 160 deg. The fractional rms errors were typically 1.5%. A liquid hydrogen target was bombarded by a beam of 2.5×10^6 mesons/sec. The scattered pions were detected by a counter telescope. Recoil protons were eliminated by means of a Cerenkov counter.

A phase-shift analysis was performed combining the above-mentioned data with the recoil-proton polarization measurements taken recently with the help of a polarized proton target. Only one acceptable SPD Fermi-type phase-shift set was found. When F waves were included, a total of three possible phase-shift solutions emerged from the analysis. However, arguments based on the data could still be made to eliminate all but one phase-shift set. On the other hand, the remaining phase-shift set, similar in type to the SPD solution, suffers from the disadvantage of large rms errors assigned to its small phase shifts.

I. INTRODUCTION

The Yukawa theory explains the long-range forces in a nucleus as the result of the exchange of pions between nucleons. This gives the investigation of the pion-nucleon interaction its fundamental importance. A traditional tool of this investigation has been the scattering of pions on hydrogen. To facilitate analysis, data at a given energy should include the recoil-proton polarization aside from the differential cross section and the total cross section. Although a considerable number of measurements exist on π^+p scattering, they are seldom ever complete or precise. The primary cause of low accuracy in many experiments was that high-intensity pion beams were not available. The most complete work up to date π^+p scattering exists at 310 MeV.[1,2] The total cross section, differential cross section, and recoil-proton polarization were measured at this energy.

This report represents part of an effort to extend this completeness to a lower energy. In this experiment we have measured the differential cross section with typically 1.5% fractional rms errors at 250 MeV nominal incident-meson kinetic energy.

The measurement of the recoil-proton polarization was accomplished in a companion experiment,[3] at the same incident-meson kinetic energy.

It is customary to present the results in terms of phase shifts $\delta_{L,2T,2J}$, which illustrate the dependence of the interaction potential on the orbital angular momentum $L\hbar$, the total angular momentum $J\hbar$, and the isotopic spin quantum number T of the pion-nucleon system.

Another motivation for this presentation arises from the expectation that a small number of parameters (phase shifts) is sufficient to describe the scattering. To support this expectation one often cites the classical relationship between the maximum orbital angular momentum, the center-of-mass momentum p, and the maximum range of nuclear forces R:

$$L_{MAX} = \frac{pR}{\hbar} .$$

Phase shifts corresponding to $L \geqslant L_{MAX}$ are assumed to decrease rapidly in magnitude, and they are therefore neglected.

For instance, at the kinetic energy of this experiment and on the assumption of one pion Compton wavelength for the maximum range of nuclear forces, $L_{MAX} \approx 2$, indicating only five nonvanishing phase shifts. This argument is obviously oversimplified, in view of the complex nature of the pion nucleon interaction. Therefore, L_{MAX} must be determined experimentally.

Because of the dominance of the $(T = \frac{3}{2}, J = \frac{3}{2})$ resonance in this energy region, the total cross section which contains only terms in $\sin^2\delta_{L,2T,2J}$, will suppress phase shifts other than the $\delta_{1,3,3}$. The total cross section was not measured in this experiment. Both the pion angular distribution and the recoil-proton polarization must be measured, however, to determine the phase shifts uniquely. This comes about because of theoretical ambiguities in the phase-shift analysis and the finite accuracy of the experimental data.

The results of $L_{MAX} = 2$ and $L_{MAX} = 3$ phase-shift analyses are presented in this report.

Inelastic scattering was neglected in the analysis. The error committed should be negligible when one compares the estimated 0.2-mb total inelastic cross section with 110 mb for the total elastic cross section at 250 MeV.

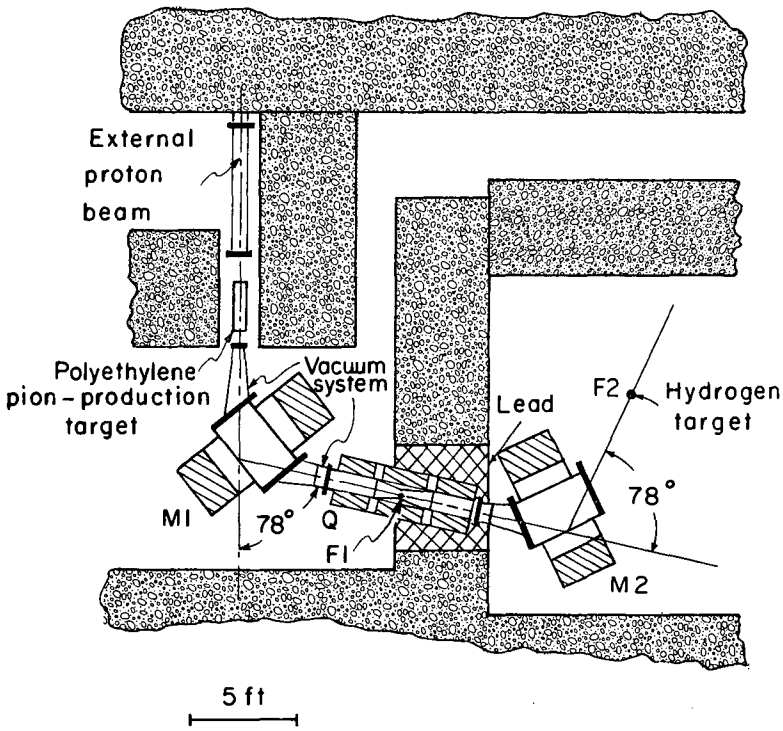

II-1. Plan view of the pion-beam spectrograph.

II. PION BEAM

A. External Proton Beam

Figure II-1 shows the plan view of the beam spectrograph. Located upstream of the main cyclotron shielding wall were a bending magnet, to steer the external proton beam through a hole in the shielding wall, and a quadrupole doublet, which focused the proton beam on the polyethylene (CH_2) production target. The proton energy and intensity were 745 ± 8 MeV and $(2 \pm 1) \times 10^{11}$ protons/sec respectively. The diameter of the beam near the production target was 2 in., determined from a short x-ray film exposure at full intensity.

B. Production of Pions

The pions were produced mainly from the reaction $p + p \rightarrow d + \pi^+$, where the target protons were those of the hydrogen in the polyethylene. The pions are monoenergetic because of the two-body final state, and remain nearly so despite the thick production target necessary for a high meson yield. This is because mesons produced in the upstream part of the target and moderated by the full length of the polyethylene have approximately the same energy as mesons produced by moderated protons at the downstream end of the target. The production cross section for pions from the competing reaction[4] $p + p \rightarrow p + n + \pi^+$ is several times that for the two-body process used. However, the small momentum band accepted by the spectrograph of this experiment limits this contribution. The length of the production target was optimized at 30.5 in. for maximum meson yield at the central momentum of the spectrograph (363.5 MeV/c).

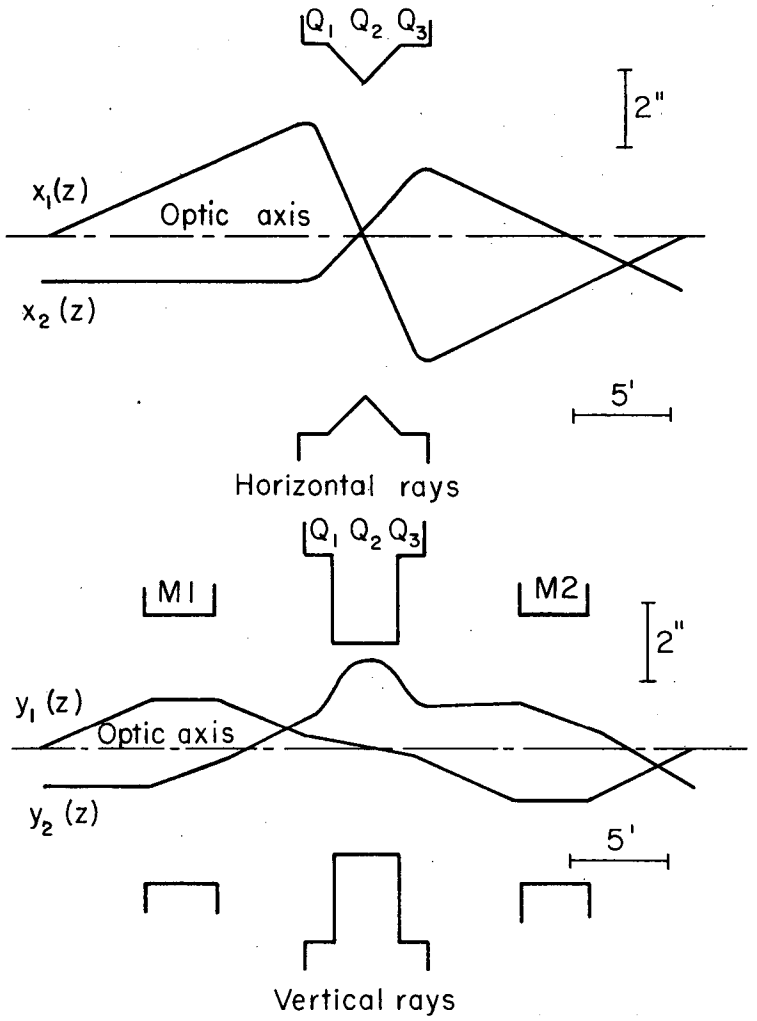

II-2. Horizontal and vertical ray diagrams.

C. Beam Spectrograph

The beam transport system, designed by R. A. Swanson,[5] consists of two bending magnets M1 and M2 and a centrally located 12-in.-aperture quadrupole triplet Q. The front and back sections of the latter provide most of the horizontal focusing. The center section has relatively little effect in the horizontal plane, because beam particles passing through it remain close to the axis of the quadrupole, i.e., its low-field region. Vertical focusing is provided by the entrance and exit regions of the bending magnets. The quadrupole triplet now serves as a field lens for the bending magnets. Horizontal and vertical ray diagrams are shown in Fig. II-2. Omission of the customary quadrupoles preceding the first and following the last bending magnet results in a reduction of overall length and therefore a gain in meson flux. The Swanson system is 32 ft long, from source to final image along the optic axis. Another gain in the meson flux is achieved through an increase of the acceptance of the system, caused by the large (12-in.) aperture of Q. The measured acceptance mean solid angle was 6.5×10^{-3} steradian over a 2-in.-diameter circle.

The operation of the beam transport system is as follows. Pions produced in the forward direction are first momentum-analyzed by the bending magnet M1 , then brought to an intermediate focus at the physical center of Q, F1 . Because of the momentum dispersion of M1 , the off-momentum foci are laterally displaced from the center of Q. Therefore, momentum definition can be obtained by placing a slit here.

In this case there was a 2-in.-wide aperture which corresponded to a momentum spread of ±3%. Protons of the central momentum were degraded by a 1-in. polyethylene absorber placed near the intermediate focus and swept out of the main beam by the bending magnet M2 . The spectrograph is symmetrical about the first focus. The second half approximately cancels the momentum dispersion of the first half, because M1 and M2 bend in the same direction and Q inverts the image at F1 . An evacuated can was placed inside the magnet system to minimize Coulomb scattering of the beam.

D. Pion Beam Characteristics at the Hydrogen Target

Starting values for the magnet currents were obtained by extrapolation along magnetization and field gradient curves from 100 MeV/c, where a wire-orbit analysis of the original Swanson spectrograph had been made. As expected from the difference between this momentum and the central momentum of this experiment (363.5 MeV/c), some adjustment of the magnet currents was found to be necessary.

The emerging pion beam at the second focus F2 , where the hydrogen target was placed, was about 2 in. wide and 1.5 in. high at the half-maximum points. Typical horizontal and vertical beam profiles are shown in Fig. II-3. The measured beam divergence at the half-maximum points was $\pm 2^{\circ}$. A maximum beam intensity of 2.5×10^{6} mesons/sec was measured by using an argon-filled ionization chamber, similar to the one described by Chamberlain et al.[6] The conversion of ionization-chamber current to meson flux was made by using the calibration of the

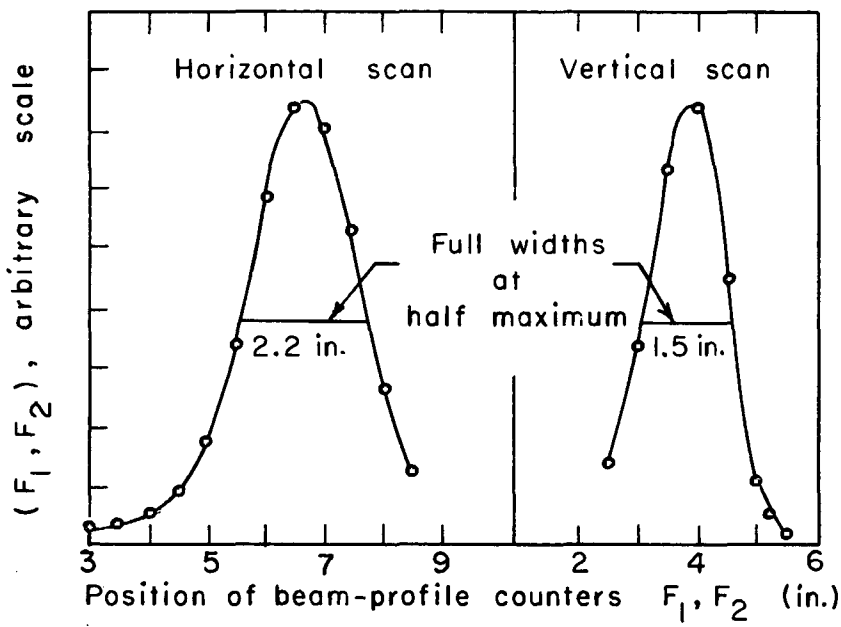

MU-34308

II-3. Typical horizontal and vertical pion-beam profiles, at the position of the hydrogen target.

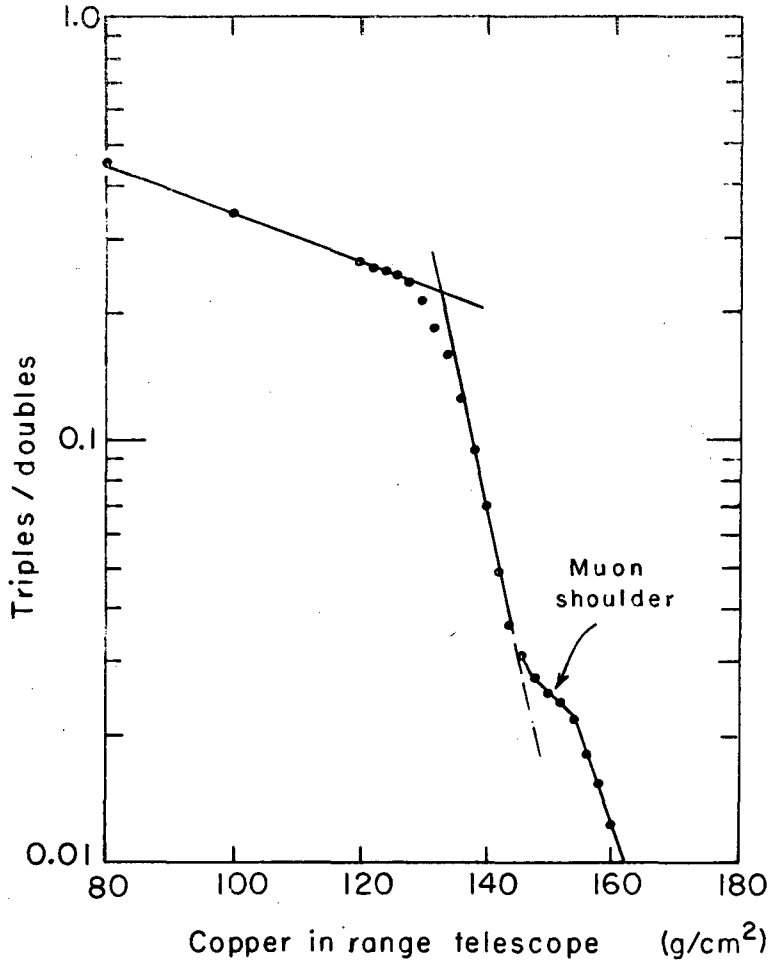

MU-34304

II-4. Integral range curve for the incident beam.

above reference. A three-counter range telescope with a variable copper absorber between the last two counters was set up repeatedly during the experiment to check on the energy of the pions at the center of the hydrogen target. The mean energy for the experiment was found to be 247.5 MeV with an rms uncertainty of ±1.5 MeV. A typical integral range curve is shown in Fig. II-4. Muons, the main beam contaminant, are clearly visible as a shoulder on the steep portion of the range curve. They are estimated at about 5% of all beam particles. The percentage of positrons is judged to be considerably smaller than the above figure. Knowledge of the exact numbers of these beam particles is not necessary here, because only a relative cross-section measurement was made and because muons and positrons do not interact strongly with protons of the hydrogen target.

Table III-I. Description of counters and related equipment.

Item	Size (in.)	Thickness (in.)
S_1	5 × 5	3/16
S_2	2-1/2 diam	3/16
S_3	5 × 5	3/16
S_4	7 × 13	1/4
S_5	10 × 20	1/4
R_1	3 × 3	1/4
R_2	3 × 3	1/4
F_1	1 × 1	1/4
F_2	1 × 1	1/4
C	4-1/2 diam	2-3/8
IC	8 diam	2

III. DIFFERENTIAL CROSS-SECTION MEASUREMENT

A. Experimental Apparatus

Following is a description of the equipment and its arrangement during this experiment.

1. Counters

Figure III-1 shows schematically the two counter telescopes used, at a typical angular setting with respect to the incident beam direction.

Counters and related equipment are listed in Table III-1. The telescope on the right of Fig. III-1, normally counting pions, consisted of four counters. The scintillation counter S_2 defined the solid angle of the telescope. For laboratory -system angles equal to or larger than 22.3 deg the solid angle was $\Omega = 0.265 \times 10^{-2}$ sr. This counter geometry will be called from here on SA (short arm).

At smaller angles than 22.3 deg, the telescope with the dimensions shown in Fig. III-1 would count too many pions of the incident beam that did not scatter in the hydrogen target. In order to keep this background tolerable, S_2 and the other counters of the pion telescope were moved farther away from the target center. The new position of S_2 was 120.75 in. from the center of the hydrogen target. The solid angle of the telescope was consequently reduced by a factor of 7.885. This counter geometry will be designated from here on LA (long arm).

Located directly behind S_2 was a water Cerenkov counter C, designed to eliminate recoil protons by counting only the pions.

Some distance in front of S_2 was another scintillation counter,

S_1. Its purpose was to reduce the solid angle of the telescope for particles that did not originate in hydrogen. The placement of S_1 represented a compromise between this purpose and the desire to keep the correction due to multiple Coulomb scattering in S_1 to a minimum. This compromise had to be modified for the small laboratory-system angles. Here the background did not reach reasonable proportions until the distance between S_1 and S_2 was increased beyond the 20.25 in. of the large-angle setup, thereby reducing the contribution from heavy materials surrounding the target. For these small angles, the separation between S_1 and S_2 was 63.3 in.

Finally, at a distance of 10 in. behind S_2 (to allow room for some carbon absorber), there was an auxiliary scintillation counter S_3. It was used for range curves of the scattered beam and in the measurement of the Cerenkov-counter efficiencies.

All pion-telescope scintillation counters were 3/16 in. thick. This thickness was the result of a compromise between the conflicting goals of a maximum particle-detection efficiency and minimum nuclear scattering in these counters. Nuclear scattering is very large in the energy range of the scattered pions in this experiment, because of the proximity to the $(T = \frac{3}{2}, J = \frac{3}{2})$ resonance. Assuming for minimum-ionizing pions a pessimistic overall conversion factor of 5 keV energy loss per photoelectron collected at the first dynode of the photomultiplier, one obtains roughly 200 photoelectrons at the first dynode. With the high-gain photomultipliers now available and the low-threshold discriminators used in this experiment, particle-detection efficiencies

close to 100% were assured.

The choice of the Cerenkov-counter thickness was faced by the same problems as those outlined for the scintillators. However, the solution to these problems was more difficult because of the low level of the Cerenkov light. Based on the frequency variation of the quantum efficiency (ratio of photoelectrons to protons) for the photomultipliers used in this experiment, one calculates $124 \times \sin^2\theta^c$ photoelectrons per inch of radiator material. Here θ^c is the angle between the normal to the Cerenkov wave front and the particle direction. At 90 deg lab, which implies $\sin^2\theta^c = 0.2465$ in water, and an estimated light collection efficiency of 25%, one obtains only about eight photoelectrons/in. on the average at the first dynode. Furthermore, for such a small average number of electrons at the first dynode the statistics of the multiplication process cannot be ignored. This further reduces the particle detection efficiency. Finally, 2-1/4 in. of water was chosen to assure a reasonable detection efficiency, even for lab angles near 180 deg.

The water was contained in a 4.5-in.-diam stainless steel cylinder with a 2-in.-diam opening in the side surface for the attachment of a Lucite light guide. Magnesium oxide (MgO) was deposited on the inside of the container. It was mixed with an acryloid resin dissolved in toluol. Upon evaporation of the solvent, the acryloid became an effective binding agent for the MgO powder.

The initially directional Cerenkov light was randomized by repeated diffuse reflection off the magnesium oxide surface. Then a fraction of

the light trapped by internal reflection in the light guide was transmitted to a photomultiplier.

A variety of "wave shifters" can be used in principle to enhance the intensity of the collected light. The particular kind given a trial prior to the experiment absorbs Cerenkov light in the ultraviolet and fluoresces in the sensitive region of the photomultiplier. The isotropic distribution of the fluorescent light helps also to decrease intensity losses by reducing the average number of reflections prior to entrance into the light guide. A concentration of 200 mg/liter of amino-G acid[7] in distilled water was tried. No appreciable shift was detected in the maximum of the pulse-height distribution due to Cerenkov light from cosmic rays. This was possibly because of dissolved oxygen in the particular sample tested. Oxygen quenches the fluorescence of the wave shifter. However, it was feared that the use of distilled water and the direct fluorescence of the amino-G acid would increase the detection efficiency for recoil protons. These were numerous and not very well known in magnitude. Therefore, tap water with no wave shifter was used during the experiment.

The telescope on the left of Fig. III-1, normally counting protons in coincidence with the pion telescope, consisted of two scintillation counters, S_4 and S_5. Their sizes and distances from the hydrogen target were chosen on the basis of the proton-to-pion solid-angle ratio with due regard to the large multiple Coulomb scattering of the slower recoil protons. S_4 and S_5 were used only during the measurement of

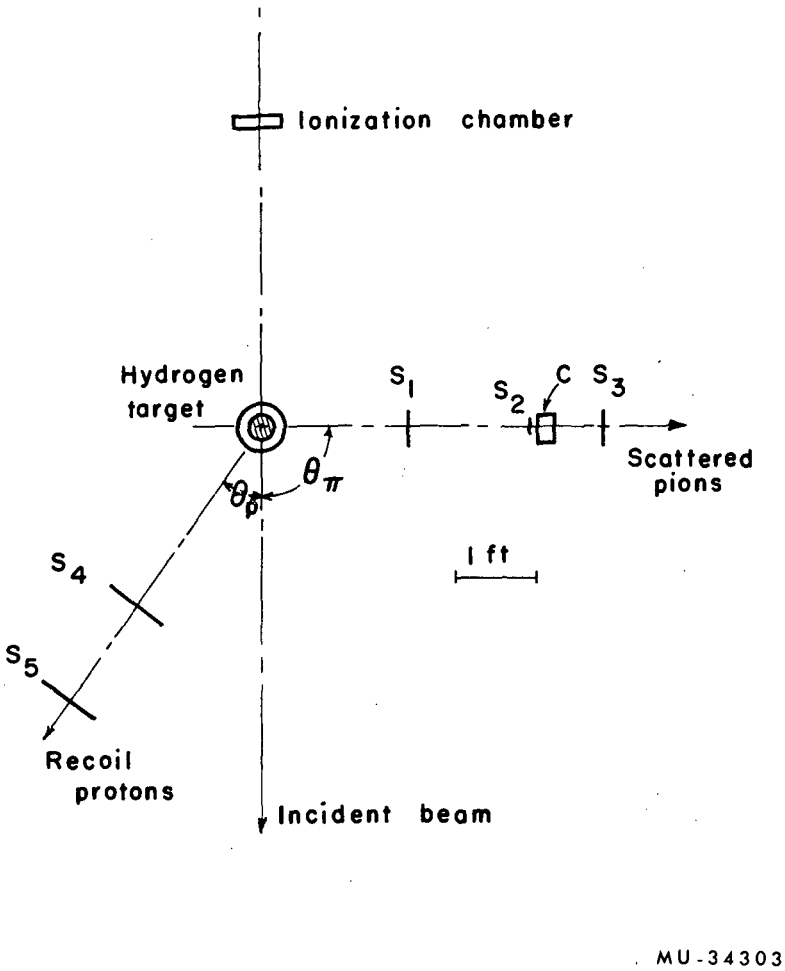

III-1. Scale drawing of the counter telescopes.

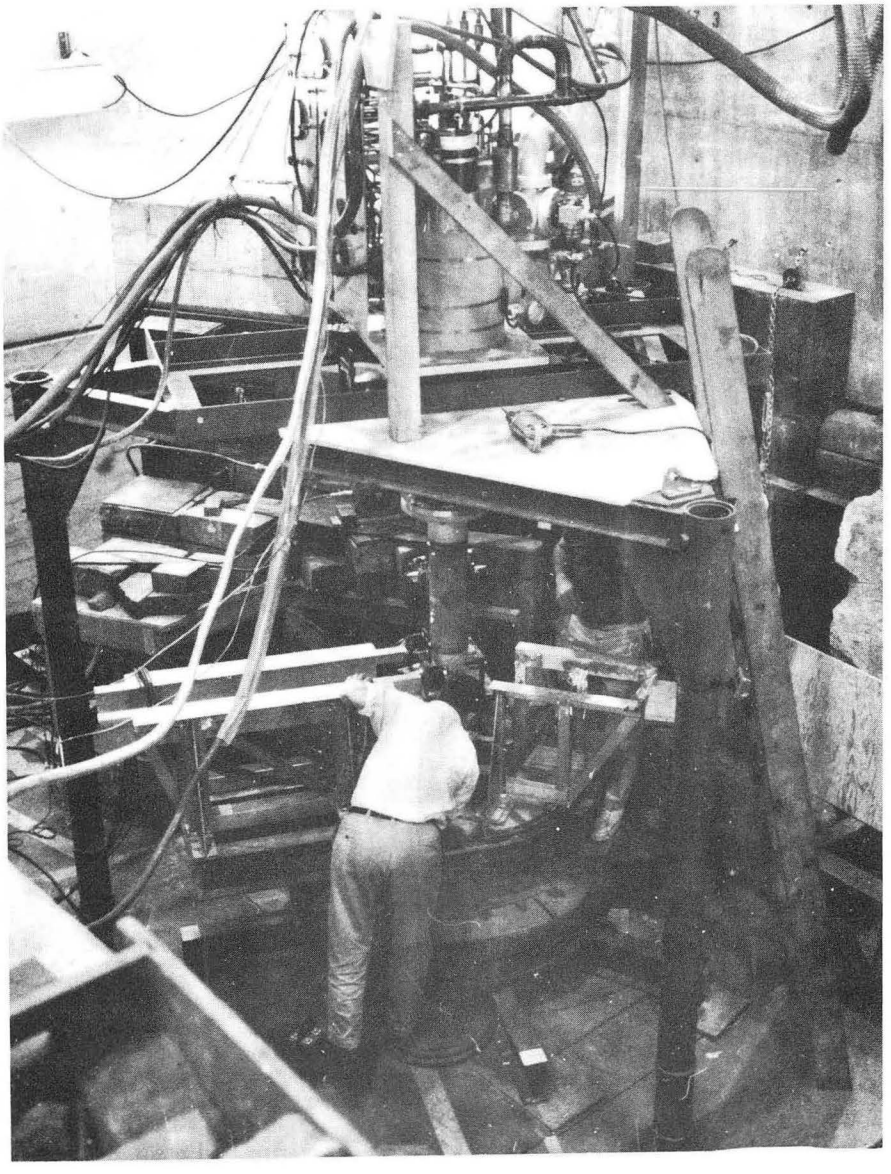

ZN-4334

III-2. Photograph of the experimental setup in the process of assembly.

the Cerenkov efficiencies.

The ionization chamber, mentioned in Chapter II, was used to monitor the incident beam.

Beam profiles at the position of the hydrogen target were obtained with the scintillation counters F_1 and F_2, in coincidence. These counters were mounted on a carriage which was driven by a remotely controlled selsyn motor. The hydrogen target was rolled out of the way at the time of this measurement.

The scintillation counters R_1 and R_2, which are not shown in Fig. III-1, were located some distance off the scattering plane to monitor the scattered beam. One-fourth of copper was placed between them to stop slow particles coming from the target walls.

Figure III-2 shows some mechanical details of the experimental setup in the process of assembly. The set of rails visible on the left was used to mount the pion-telescope counters. The light guide of S_2 alone was directed upward to prevent coincidences arising from Cerenkov light in the Lucite of the light guide. The rail support was rigidly attached to a naval gun mount which could be rotated in increments of 0.1 deg over a large range of scattering angles. The counters of the proton telescope were mounted in similar fashion. The rail support for that telescope, shown on the right of Fig. III-2, could be rotated independently of the pion telescope but around a common axis of rotation.

2. Hydrogen Target

Liguid hydrogen was contained in a 3-in.-diam 6-in. upright

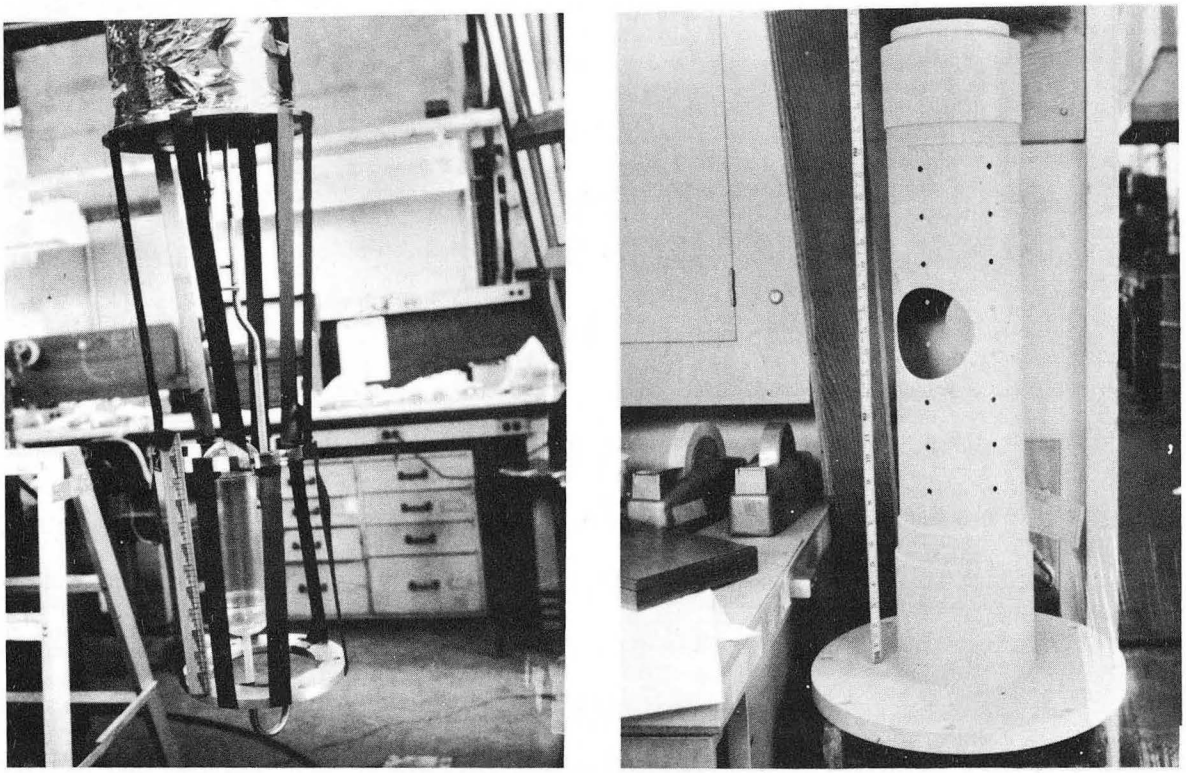

ZN-4335

III-3. Photographs showing the hydrogen flask and the vacuum jacket.

cylinder, made of 0.0075-in. Mylar. To prevent heat transfer to the Mylar flask, the latter was placed inside an evacuated 6-in.-diam aluminum can. The thickness of a portion of the can, roughly 7 in. above and below the beam line, was kept down to 0.061 in. Four-in. windows were cut into this vacuum jacket along the beam line and the aluminum was replaced by Mylar wrapping. For maximum strength and minimum thickness it was decided to use several continuous layers of Mylar glued together rather than one sheet of solid material. After the experiment, the Mylar wrapping was cut open to determine its exact thickness for purposes of data correction. The average thickness was found to be 0.0347 ± 0.0014 in.

Radiative heat transfer was reduced first by two sheets of 0.00025-in. aluminum wrapped around the flask and then by a 0.003-in. aluminum cylinder separated with 1/4-in. Styrofoam spacers from the flask.

Flask and vacuum jacket are shown in Fig. III-3. The assembled hydrogen target and its mounting can be seen in the center of Fig. III-2.

A check was also made on the actual position of the flask within the vacuum jacket. Of particular interest was an up- or downstream displacement, since a position error perpendicular to the incident beam could be cancelled out to first order by left-right averaging of the differential cross section. x-Ray photographs of the hydrogen target both with full and with empty flask showed no measurable systematic error.

3. Electronics

All scintillators were viewed by RCA-7264 photomultipiers. These

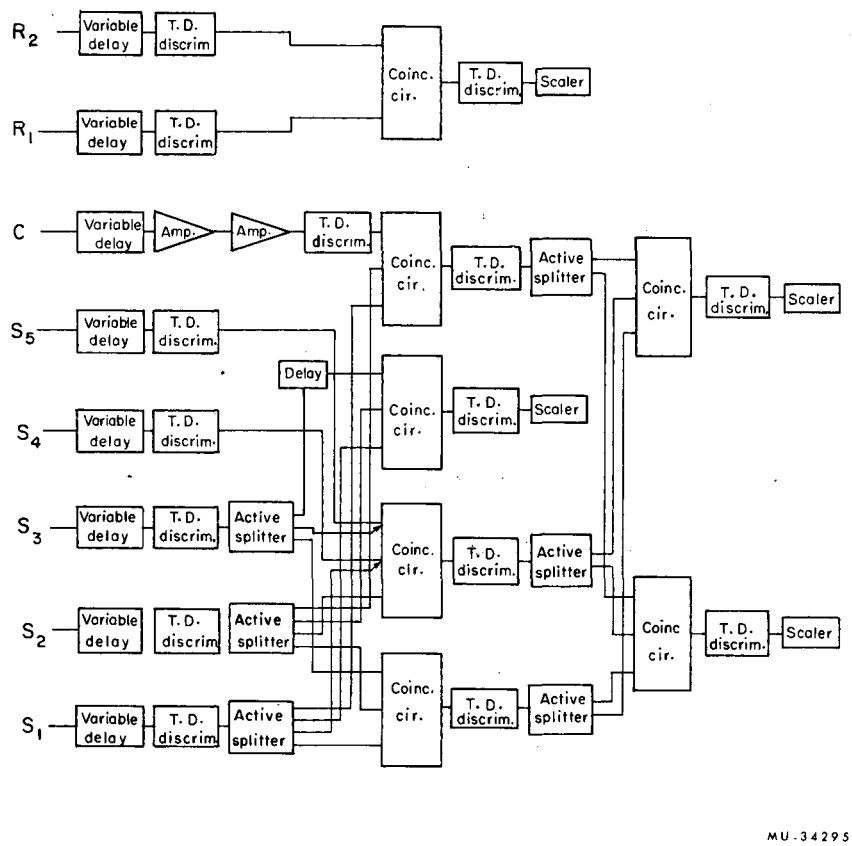

III-4. Block diagram of the electronics used during the experiment.

tubes have a small transit-time spread owing to their curved photocathode design. A standard RCA-6810A tube was chosen for the Cerenkov counter. Timing uncertainties due to the low level of the Cerenkov light made the consideration of the photomultiplier transit-time spread less important for that counter. However, the particular tube was selected for low inherent noise and high gain at low anode voltage.

Anode voltages for the scintillator tubes were preset to yield 1-volt pulses, using the roughly 1-MeV γ rays of a Co^{60} source; 1 MeV was also the ionization loss for fast pions in the polystyrene of the scintillators. The anode voltage for the Cerenkov tube was set initially on the basis of a pre-experiment measurement of the particle-detection efficiency for cosmic-ray muons. All voltages were modified during the experiment, with scattered pions as test particles.

Figure III-4 shows the block diagram of the electronic circuits used during the experiment. Not all the logical functions indicated were used at all times. Some were changed later to duplicate other critical coincidences for reasons of reliability.

Photomultiplier pulses were first delayed relative to each other with variable lengths of RG-63 cable. Then, with the exception of the Cerenkov pulses, they were fed into "constant-delay"[8] tunnel-diode discriminators. Cerenkov pulses were first amplified by two HP-460A wide-band amplifiers.

Normally, a direct input to the coincidence circuits would have been preferred, had it not been for the availability of the constant-

delay discriminators, which were designed for minimum variation of delay over a wide range of input amplitudes. These discriminators introduced very little slewing at input amplitudes larger than 0.8 V, even for high threshold settings. The actual settings were 0.25 V for the scintillator channels and 0.15 V for the Cerenkov channel.

The outputs from this initial pulse-shaping stage were then routed to the appropriate transistorized coincidence circuits of the Wenzel type.[9] Whenever more than one output from a particular discriminator was needed an active splitter was used. Such a splitter consisted of four parallel emitter-followers with a common input.

Between the coincidence circuits and the conventional scaling units another discriminator stage was inserted to prevent feedthrough from activating the scalers. These tunnel-diode discriminators were of a less elaborate kind, which was justifiable considering the two preceding stages of pulse shaping.

The "dead time" of the discriminators in the first pule-shaping stage was 50×10^{-9} sec. Since total singles rates were never larger than 10^4/sec, counting losses due to this cause were negligible.

B. Experimental Method

1. Cerenkov Efficiencies

A considerable amount of the experimental time available was spent on the accurate measurement of the Cerenlov detection efficiencies for pions and protons.

The efficiency for pions was expected to vary rapidly with pion

velocity. Therefore, it was measured at most of the same laboratory-system angles as the differential cross section. Below 90 deg lab, the upper kinematic limit for recoil protons, hydrogen-scattered pions were selected by counting in coincidence with conjugate protons. This arrangement is seen in Fig. III-1. The efficiency was determined by taking the ratio of coincidences $S_1S_2S_3S_4S_5C$ to $S_1S_2S_3S_4S_5$, after background subtraction. Laboratory-system angles smaller than about 45 deg could not be covered by this method, because too many conjugate protons were stopping in the target walls. For angles larger than 90 deg the pion-efficiency measurements were continued by recording the ratio of coincidences $S_1S_2S_3C$ to $S_1S_2S_3$, again after background subtraction. The same scheme was also used to get a reference point at the incident pion energy. For that purpose the pion telescope was placed into the incident beam, at a drastically reduced level, and the hydrogen target was rolled out of the way.

At 90 deg before measurements were started the Cerenkov anode voltage and the gain of the following amplifiers were increased until a plateau in the pion efficiency was reached.

Since recoil protons could cause scintillation, either in water or the surrounding magnesium oxide, the detection efficiency for protons had to be determined also. Furthermore, recoil protons could produce fast electrons by knock-on, which in turn could have been the source of unwanted Cerenkov light.

The measurement was made by reversing the roles of the two counter telescopes. The pion telescope was counting protons and the proton

telescope counted the conjugate mesons. As before, the ratio of sixfold to fivefold coincidences was recorded.

Range calculations predicted that protons would stop in the Cerenkov counter at 37.7 deg. Also, no δ rays were expected above the Cerenkov threshold at angles larger than 30 deg. Therefore, only three forward angles were covered, with an upper limit at 34.9 deg.

2. Scattering Data

Our desire to obtain an accurate angular distribution for pion-proton scattering conflicted with some of the requirements of an absolute measurement of differential cross section. Therefore, we decided to restrict this work to the measurement of the relative differential cross section ("angular distribution"). Then, before our data were directly useful, they had to be fitted to total cross-section values taken from other experimental work.

The number of incident pions in the beam was measured by allowing an ionization chamber to deposit its charge on a capacitor and recording the capacitor potential in volts. I_o is used here to denote the number of "ion volts" (I.V.) -- volts accumulated on our capacitor in a given beam exposure. Since we have sought only a relative differential cross section measurement, it has not been necessary to calibrate this beam detector with great accuracy; I_o is simply used as a constant proportional to the number of incident pions in the beam in any given beam exposure. $I(\theta)$, the number of pions scattered into the solid angle of the counter telescope, was detected by the coincidence S_1S_2C . The contribution from the target walls was eliminated by taking the difference between

target-full and target-empty rates. Under ideal circumstances this difference is proportional to the differential cross section:

$$\frac{d\sigma}{d\Omega}(\theta) \propto (I(\theta)/Io)\ \text{FULL} - (I(\theta)/Io)\ \text{EMPTY}$$

The angular distribution was measured at thirteen angular positions between 14.9 deg and 160 deg in the center-of-mass system.

Some consideration was given prior to the experiment to a check on the background subtraction by counting only those pions which produced coincident recoil protons in S_4 and S_5. However, the angular region where this check would have been possible was unfortunately limited to lab angles at which the background was small, i.e., around 90 deg. At smaller pion angles, recoil protons scatter too much in the target for this method to be successful without additional corrections.

The ratio of the background to the hydrogen effect varied for most angles between 0.3 and 0.5. Only the most forward angles of 14.8 deg and 11.0 deg lab had the exceptionally high ratios of 1.6 and 5.8 respectively.

Many precautions were taken to search for and minimize systematic errors.

The incident beam was scanned periodically to center it on the target. Also, range curves of the incoming particles were often examined to maintain a constant pion energy at the center of the target. Finally, except at very small and very large angles, scattered pions were counted to the left and right of the incident beam direction. At 22.3 deg, the smallest angle at which this method was feasible, the difference between

the left and right averages was only 1.7% for the hydrogen effect, although the left background was almost twice the right background. This difference was not significant considering the error assigned to the data at this angle.

In order to detect systematic drifts in the scattering data, measurements were returned repeatedly to a check angle established at 37.7 deg. Consistency plots at this angle showed no systematic changes. However, the individual points were scattered about the average more than the errors assigned to them on the basis of simple Poisson statistics would justify. This point is discussed further in Chapter IV.

A running check was kept with the stationary monitors R1 and R2 to detect differences between successive flask-full or flask-empty conditions. Only normal fluctuations were found.

Part of the raw data was collected at about 1/5 of full beam because of safety requirements imposed by nearby construction. Intermediate changes in the beam level were also introduced deliberately at 22.3 deg. No significant differences indicating a rate dependence were observed.

An estimate of the accidental rate for a threefold coincidence was obtained by delaying the output from S_3 by 52×10^{-9} sec and combining it with S_1 and S_2. This delay corresponds to the separation between rf pulses of the Berkeley cyclotron. The accidental rate was never larger than 0.3% of the scattered pion rate.

The performance of the electronic components was also checked. Counter voltage plateaus and relative delays were examined repeatedly.

Corrections for nuclear scattering in the counters of the pion telescope were obtained by placing additional dummy counters in the scattered beam. These measurements were only attempts to provide a rough guide to the numerical corrections which were to follow. For the scintillators the effect was small. Therefore, the statistical accuracy of the measured correction was low. For the dummy Cerenkov counter there was a complicating geometical effect caused by the appreciable thickness of this counter.

IV. DATA REDUCTION

A variety of corrections was necessary to account for the departure from the ideal case, in which the differential cross section is exactly proportional to the net (S_1S_2C) coincidence rate.

Some pions were lost by second nuclear scattering in hydrogen itself, in the target walls, and in the counters of the pion telescope. Then, because of the sizable separation of the defining counter from the target, some pions decayed in flight. The efficiency of the Cerenkov, less than 100%, caused a further reduction in the counting rate of the scattered pion flux. Finally, there was a small geometrical correction due to the finite target volume and finite detector area.

Application of these corrections to the basic (S_1S_2C) rate yields, for the differential cross section, the expression

$$\frac{d\sigma}{d\Omega} = \frac{(1-f_p)(S_1S_2C)_{NET}}{(1-f)\epsilon\ g\ I_o'\ N(\Delta\ \Omega)} \quad , \qquad (4.1)$$

where $(S_1S_2C)_{NET}$ represents the background-subtracted number of threefold coincidences, normalized to ion volts; and f_p is the number of protons counted by the Cerenkov, expressed as a fraction of the total rate in this counter. The fraction of pions lost by second nuclear scattering and pion decay is given by f (higher-order scattering was neglected); ϵ is a generalized efficiency of the Cerenkov, calculated for scattered particles other than protons; g represents the geometrical correction.

Not shown explicitly is a small correction applied at the two most forward angles to compensate for the attenuation of the background by

the target hydrogen.

The remaining factors are: I_o' , the number of incident pions per ion volt; N , the number of proton scatterers per cm^2; and $\Delta\Omega$, the solid angle of the pion telescope. These normalizing factors are independent of the scattering angle. Knowledge of their exact magnitude was not necessary, because the normalization (to mb/sr) was obtained from a previously known total cross section by integration.

The following approach was taken to arrive at an angular distribution which is exactly proportional to the differential cross section at all pion scattering angles:

(a) All protons scattered into the pion counter telescope were treated separately.

(b) Corrections were made to the $(S_1S_2C)_{NET}$ counting rate to obtain the equivalent of a 100% Cerenkov-counter efficiency for all mesons.

(c) Small corrections were applied to the rate resulting in (b) in order to account for rescattering of mesons in the hydrogen target and in other parts of the apparatus.

(d) A small correction was added to those in (c) for pions that decayed in flight.

(e) Finally, a small correction was made for the variation of the differential cross section resulting from a finite target volume and a finite detector area.

Although this list indicates the program according to which the corrections were made, the order in which the details of these corrections are presented in the subsequent sections is somewhat different for

reasons of convenience. Final results are given in Section E.

A. Multiple Nuclear-Scattering Corrections

Only second-order interactions were considered. E.g., pions that interacted the second time in hydrogen were assumed not to scatter again until they reached the middle of the defining counter S_2.

On the basis of this assumption, the relation at a given laboratory-system angle between the true scattering rate I/I_o and the doubles rate for mesons $(S_1S_2)_M$ is

$$\frac{I}{I_o} = \frac{(S_1S_2)_M}{(1-f)} = \frac{(S_1S_2)_M}{1-(f_\pi^{H,NET} + f_\pi^{W,NET} + f_\pi^{S,NET} + f_\mu^{NET})} \quad . \qquad (4.2)$$

This expression serves to relate f, the fraction of pions lost ahead of the center of S_2, to its contributions from the various second-order processes. $(S_1S_2)_M$ is defined in Section C, Eq. (4.11) in terms of the measured rate $(S_1S_2C)_{NET}$. The superscripts H, W, and S followed by NET indicate a net loss due to scattering in hydrogen, target walls, and counter material respectively; f_μ^{NET}, the net fraction of pions lost by decay into muons, is also included.

Following is a description of the components of f due to second nuclear scattering.

1. Hydrogen-Hydrogen

The thin-target approximation was used in the calculation of this correction. All first interactions were assumed to occur at the center of the target. The fraction of pions scattered out of the counter telescope, $f_\pi^{H,OUT}$, was given by the joint probability of first scattering into the solid angle of the counter telescope followed by second scattering in all directions, whereas $f_\pi^{H,IN}$, the fraction of pions scattered into the counter telescope, was taken as the joint probability for first scattering into a given solid-angle element followed by

Table IV-I. Results of second nuclear scattering in hydrogen.

θ_{LAB} (Deg)	H, OUT $f\pi$ (%)	H, IN $f\pi$ (%)	H, NET $f\pi$ (%)
11.0	1.88 ± 0.07	0.99 ± 0.03	+0.89 ± 0.08
14.8	1.91 ± 0.07	1.02 ± 0.03	+0.89 ± 0.08
22.3	2.02 ± 0.07	1.13 ± 0.03	+0.89 ± 0.08
37.7	2.39 ± 0.09	1.59 ± 0.04	+0.80 ± 0.09
54.2	2.86 ± 0.10	2.68 ± 0.05	+0.18 ± 0.11
72.2	3.14 ± 0.11	4.68 ± 0.17	-1.54 ± 0.20
92.1	2.49 ± 0.09	4.99 ± 0.35	-2.50 ± 0.37
114.4	1.48 ± 0.05	3.62 ± 0.27	-2.14 ± 0.27
126.5	1.25 ± 0.05	3.17 ± 0.23	-1.92 ± 0.24
152.5	0.97 ± 0.03	2.74 ± 0.20	-1.77 ± 0.20

a second scattering into the solid angle of the counter telescope, summed over all directions of first scattering.

Attenuation of the incident and scattered meson flux in hydrogen could be neglected because a relative angular distribution was the only object of this experiment.

The net scattered-out fraction of pions $f_\pi^{H,NET}$ is given by

$$f_\pi^{H,NET}\frac{I}{I_o} = \left(f_\pi^{H,OUT} - f_\pi^{H,IN}\right)\frac{I}{I_o} = \frac{N^2}{2}\,\sigma_1(\theta)\,\sigma_{TOT}(\theta)\Delta\Omega \qquad (4.3)$$

$$- \frac{N^2}{2}\int \sigma_1(\alpha)k_2(\alpha)\sigma_2(\beta)d\Omega_\alpha\Delta\Omega\ ,$$

where the true scattering rate I/I_o was approximated by

$$I/I_o = N\sigma_1(\theta)\Delta\Omega\ . \qquad (4.4)$$

Here $N = 2.845 \times 10^{23}$ protons/cm^2 (it was obtained from the hydrogen density and the target thickness, averaged over the horizontal beam distribution); θ is the polar angle of the pion counter telescope; the angle for first scattering is α, and the angle for second scattering is β, measured between the direction for first scattering and the direction of the counter telescope; σ_1 and σ_2 are the π^+-p laboratory-system cross sections for first and second scattering, respectively; $\sigma_{TOT}(\theta)$ is the total cross section for π^+-p scattering. It depends implicitly on the angle θ through the kinetic energy of the first-scattered pion. Published experimental data[10] were used for all cross sections.

Although the number of scatterers available for second scattering is on the average $N/2$ for a thin target, a factor $k_2(\alpha)$ was applied

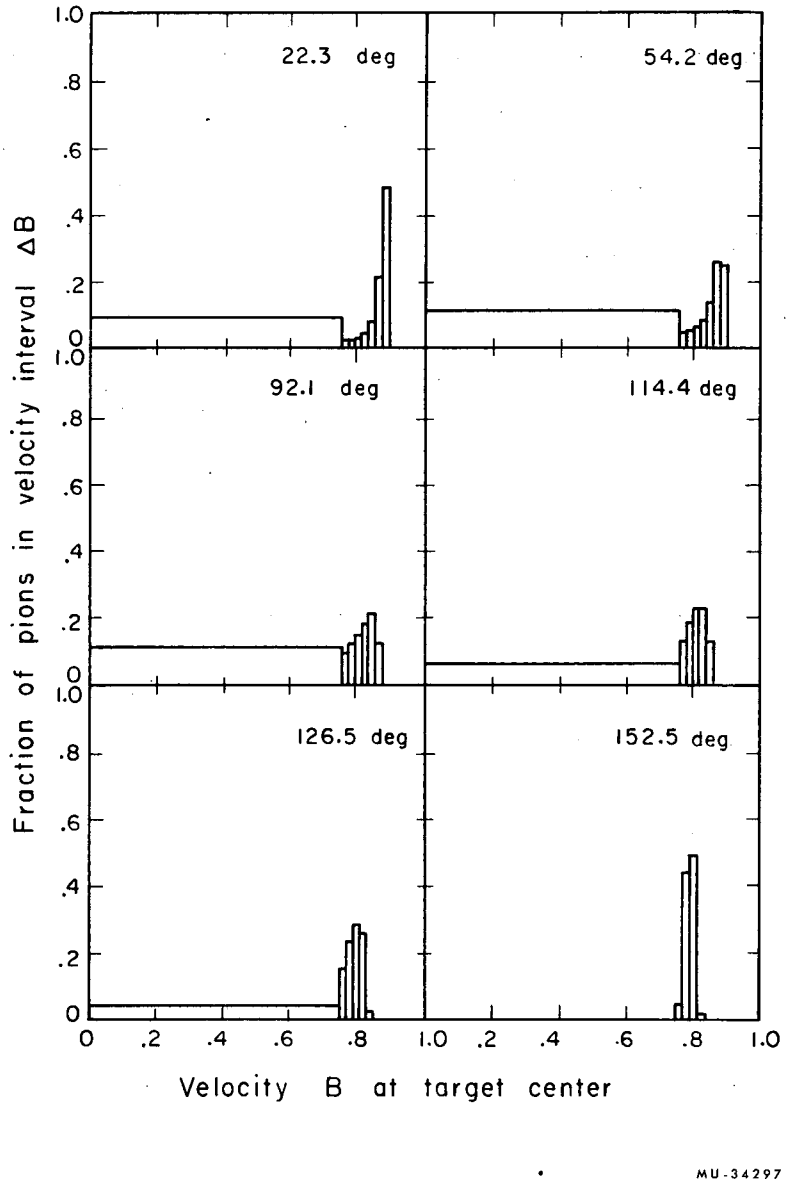

IV-1. Velocity distribution of second-scattered pions in in hydrogen at six selected counter-telescope angles.

to express the variation of the scattering length with the angle of first scattering: $k_2(\alpha)$ is the ratio of the actual scattering length, measured from the center of the target, to the radius of the hydrogen flask.

The net fraction of pions lost $f_\pi^{H,NET}$, as well as its components $f_\pi^{H,IN}$ and $f_\pi^{H,OUT}$, are given in Table IV-I for the laboratory-system angles of the experiment. The velocity distribution of the scattered-in pions, which was necessary for the calculation of the generalized Cerenkov efficiency ϵ, is given for six selected lab angles in Fig. IV-1. The subdivision of the velocity interval below $B = 0.75$ was not necessary because of the Cerenkov threshold at that velocity.

Computational errors were minimized by the use of a digital computer which was programmed to calculate this correction with a precision limited only by the uncertainties in the experimental data. To find the effect of these input errors on $f_\pi^{H,IN}$ and $f_\pi^{H,OUT}$, both the incident pion energy and the cross section data were independently raised and lowered by one standard deviation. The two effects were then combined in quadrature. The results are the errors assigned to $f_\pi^{H,IN}$ and $f_\pi^{H,OUT}$ in Table IV-I.

2. Hydrogen-Target Walls

Second scattering for these pions occurred at the walls of the target. Therefore, it was necessary to consider the finite extent of the target.

The drawing in Fig. IV-2 shows the geometry of the outer target wall (vacuum jacket) and the SA (short arm) counter telescope. The

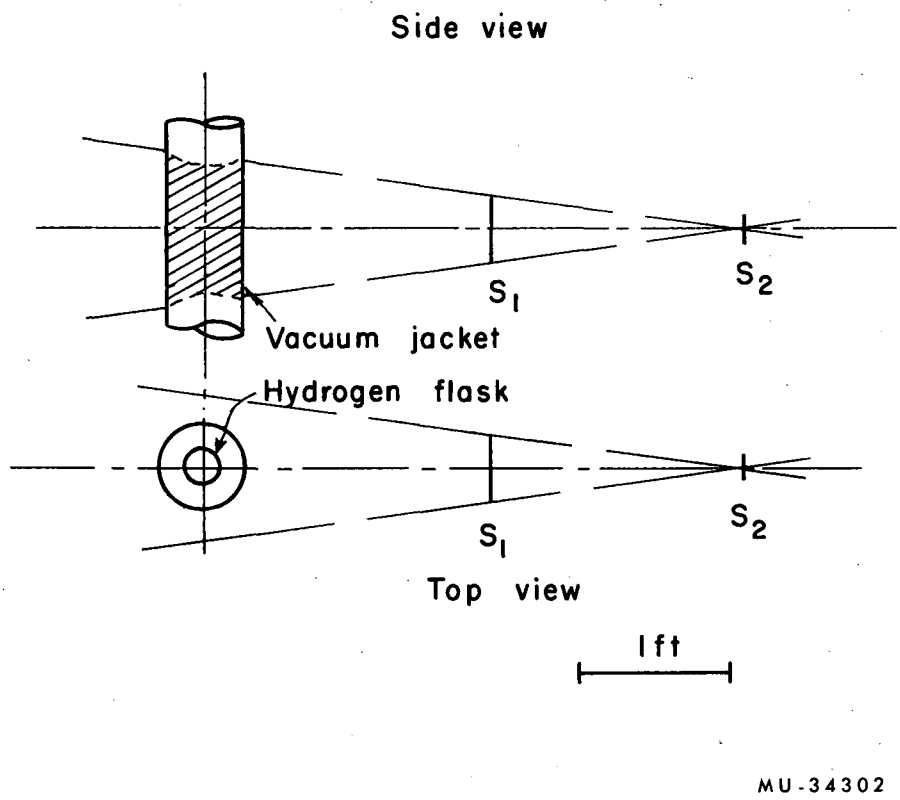

IV-2. Scale drawing of the short scattering arm (SA) counter arrangement with geometrical limits on the calculation of the second-scattering correction in the target walls.

Table IV-II. Number of scatterers/cm^2 available for second scattering in the target walls.

Radius (in.)	Material	Element	Number of scatterers x 10^{20}(cm^{-2})
1.5	Mylar	Carbon	8.25
		Oxygen	3.30
		Hydrogen	6.60
3.0	Aluminum	Aluminum	93.4
	Mylar	Carbon	38.2
		Oxygen	15.3
		Hydrogen	30.5

dashed outline on the target is the intersection of a cone defined by the counters S_1 and S_2 with the target. Only pions scattering in from the shaded surface were considered.

Again, the net fraction of pions lost by scattering in the walls $f_\pi^{W,NET}$ can be written as a difference between the scattered-out and scattered-in fractions, $f_\pi^{W,OUT}$ and $f_\pi^{W,IN}$, respectively:

$$f_\pi^{W,NET}\frac{I}{I_o} = \left(f_\pi^{W,OUT} - f_\pi^{W,IN}\right)\frac{I}{I_o} = N_1\sigma_1(\theta)\Delta\Omega\sum_i N_2^{\,i}\sigma_{TOT}^{\,i}(\theta) \qquad (4.5)$$

$$-\int N_1\sigma_1(\alpha)k_2(\alpha)\sum_i N_2^{\,i}\sigma_2^{\,i}\,(\beta)\Delta\Omega d\Omega_\alpha \quad .$$

The true scattering rate I/I_o is again approximated by Eq. (4.4). As before, $N_1 = 2.845 \times 10^{23}$ protons/cm^2; $N_2^{\,i}$ refers to the number of nuclei/cm^2 for the ith element of the target-wall materials. Table IV-II shows a list of the $N_2^{\,i}$ as a function of the radial distance from the target center line.

The explanation of the remaining terms in Eq. (4.5) is identical to that for the previous correction, with the exception of the cross sections dealing with complex nuclei, σ_2 and σ_{TOT}.

Inelastic scattering events were divided into two groups. In the first group were absorption and charge exchange, for which the final-state particles were primarily protons, neutrons, and neutral pions. None of the protons was fast enough to count in the Cerenkov and neutrons could be counted only by another charge-exchange interaction. Since neutral pions were few, this meant that interacting pions in this group

Table IV - III. Results of second nuclear scattering in the target walls.

θ LAB (Deg)	Counter geometry	f_π^W, OUT (%)	f_π^W, IN (%)	f_π^W, NET (%)
11.0	LA	0.53	0.29	+0.24
14.8		0.53	0.29	+0.24
22.3		0.54	0.31	+0.23
22.3	SA	0.54	0.32	+0.22
37.7		0.56	0.50	+0.06
54.2		1.65	0.92	+0.73
72.2		1.65	1.31	+0.34
92.1		1.54	1.43	+0.11
114.4		1.47	1.17	+0.30
126.5		1.43	1.01	+0.42
152.5		0.44	0.72	-0.28

had a negligible probability of being counted as mesons in the counter telescope.

In the second category of inelastic processes was quasi-elastic scattering with positive pions of reduced energy in the final state.

Published experimental data were used to obtain total absorbtion cross sections as well as the angular distributions for quasi-elastic pions.[11-21]

Diffraction scattering was handled with experimental data[22,23] up to 150 MeV incident pion kinetic energy. Above 150 MeV it was found that scattering amplitudes based on the optical model[24,25] of the complex nucleus were an adequate approximation.

Results for this correction are presented in Table IV-III. They depend slightly on the two counter-telescope geometries LA and SA. The sudden jump in $f_\pi^{W,OUT}$, and to a lesser extent in $f_\pi^{W,IN}$, at 54.2 deg and 152.5 deg is caused by the boundary of a 4-in. window cut into the vacuum jacket along the beam direction.

No errors were assigned, because this correction was small. Neither was a velocity distribution calculated for the scattered-in pions.

3. Hydrogen-Counter Materials

This correction deals with pions which scattered the second time in the counter S_1 and 1/2 of the defining counter S_2.

The basic expression for the net fraction of scattered-out mesons $f_\pi^{S,NET}$ remains unchanged from the preceding case, Eq. (4.5). However, the formula for $f_\pi^{S,IN}$ can be simplified this time because of the small solid angle subtended by S_1 at the center of the target.

Table IV-IV. Number of scatterers/cm^2 available for second scattering in the counters S_1 and S_2.

Counter	Material	Element	Number of scatterers $\times 10^{22}(cm^{-2})$
S_1	Polystyrene	Carbon	2.34
		Hydrogen	2.34
S_2	Polystyrene	Carbon	1.17
		Hydrogen	1.17

Table IV-V. Results of second nuclear scattering in the counters S_1 and S_2

θ LAB (deg)	Counter geometry	$f_\pi^{S,OUT}$ (%)	$f_\pi^{S,IN}$ (%)	$f_\pi^{S,NET}$ (%)
11.0	LA	1.95	0.04	+1.91
14.8		1.96	0.04	+1.92
22.3		2.00	0.04	+1.96
22.3	SA	2.00	0.28	+1.72
37.7		2.09	0.26	+1.83
54.2		2.16	0.23	+1.93
72.2		2.17	0.20	+1.97
92.1		2.08	0.19	+1.87
114.4		1.79	0.19	+1.60
126.5		1.69	0.17	+1.52
152.5		1.54	0.14	+1.40

Consequently, the variation of the differential cross section with the angular coordinates of the first scattering was neglected. Also, the integration was replaced by a summation in units of solid angle, each equal in magnitude to that defined by the counter S_2 :.

$$f_\pi^{S,NET} = f_\pi^{S,OUT} - f_\pi^{S,IN} = \sum_i N_2^i \sigma_{TOT}(\theta) - \sum_{m,n} C_{m,n} \sum_i N_2^i \sigma_2^i(\beta_{m,n}) \Delta\Omega_{m,n} \ . \tag{4.6}$$

The subscripts m,n are labels for the elementary solid angles; c_m,n are constants, used to weight the contributions from these solid angles to the fraction of scattered-in pions.

Table IV-IV presents a list of the number of scatterers per cm^2, N_2^i . Results of the calculation are given in Table IV-V, again without errors.

B. Pion-Decay Correction

Another source of counting-rate losses are those pions which decay in flight. Quantitatively, the loss is described f_μ^{NET} , the difference between the fraction of pions f_μ^{OUT} , which decay before reaching the counter S_2 , and fraction of decaying pions f_μ^{IN} , which count in S_1 and S_2 by means of their final-state muons. Ignoring the non isotropic angular distribution of the pions, one can write, for f_μ^{NET} at the pion telescope angle θ ,the expression

$$f_\mu^{NET} = f_\mu^{OUT} - f_\mu^{IN} = \left(1-\exp\left[-\frac{\ell}{\lambda}\right]\right) - \frac{1}{\Delta\Omega}\iint \frac{1}{\lambda(\alpha)} \exp\left[\frac{-\ell}{\lambda(\alpha)}\right] \int P(\alpha,\beta)\, d\Omega_\beta\, d\ell\, d\Omega_\alpha \ . \tag{4.7}$$

The distance to the point of decay is ℓ ; λ is the mean decay length,

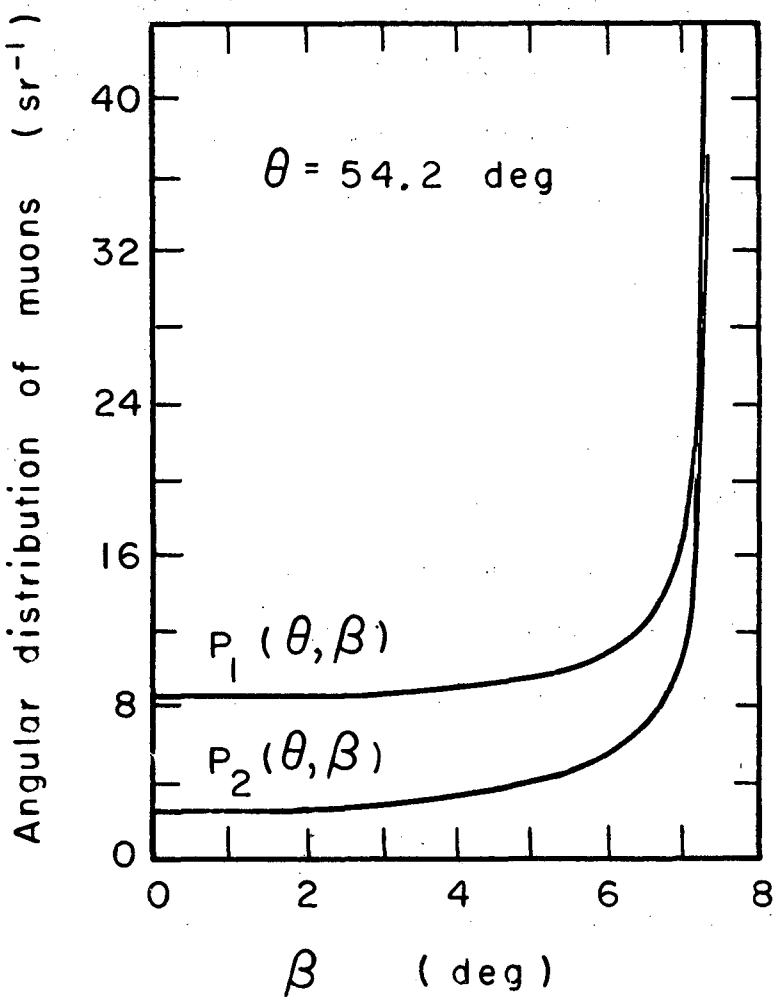

MU-34305

IV-3. Plots of the two contributions $P_1(\theta, \beta)$ to the total angular distribution $P(\theta, \beta)$ at the pion scattering angle of θ=54.2 deg. $P_1(\theta, \beta)$ are given by the first and second terms of Eq. (4.8) respectively.

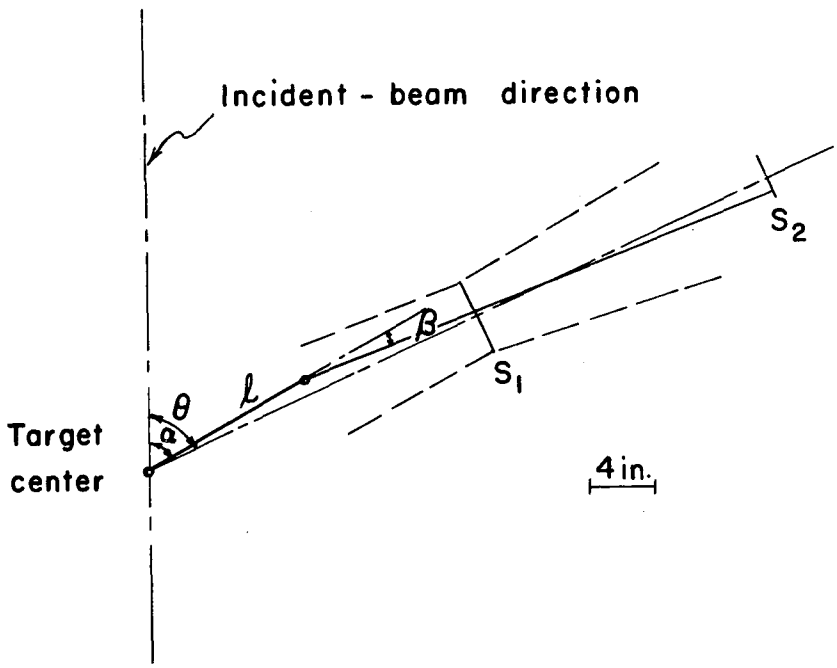

MU-34301

IV-4. Scale drawing of the principal counter geometry (SA), showing the variables of integration used in the calculation of the fraction of decayed pions that send muons back into the counter telescope.

which varied between 421 in. and 770 in., depending on the pion scattering angle α. $P(\alpha,\beta)$ is the differential distribution of muons in sr^{-1}. For a given muon emission angle β it has contributions from two center-of-mass angles β_1^* and β_2^*, corresponding to muons emitted forward and backward respectively in the pion rest frame. $P(\alpha,\beta)$ can be written

$$P(\alpha,\beta) = \frac{1}{4\pi}\frac{1}{p_\mu^{*3}}\left[\frac{p_\mu^3(\beta_1^*)}{E_\pi(\alpha)+\frac{p_\pi(\alpha)}{B_\mu^*}\cos\beta_1^*} + \left|\frac{p_\mu^3(\beta_2^*)}{E_\pi(\alpha)+\frac{p_\pi(\alpha)}{B_\mu^*}\cos\beta_2^*}\right|\right]. \tag{4.8}$$

Starred quantities are given in the pion rest frame. The momenta of the pion and muon are p_π and p_μ respectively; E_π is the total energy of the pion; $B_\mu^* = 0.2715$ is the rest-frame velocity of the muon. The two laboratory-system momenta of the muon can be obtained from the formula

$$p_\mu = \sqrt{(E_\pi E_\mu^* + p_\pi p_\mu^* \cos\beta^*)^2 - m_\mu^2}\ , \tag{4.9}$$

where $E_\mu^* = 0.7864$ is the total rest-frame energy of the muon and $m_\mu = 0.7569$ is the rest mass of the muon, both in units of the pion rest mass. Finally, the center-of-mass emission angles of the muon are given for the corresponding lab angle β by

$$\cos\beta_{1,2}^* = \frac{-\frac{B_\pi}{B_\mu^*} \pm \sqrt{1-\left[\left(\frac{B_\pi}{B_\mu^*}\right)^2 - 1\right] E_\pi^2 \tan^2\beta}}{1+E_\pi^2\tan^2\beta}\ , \tag{4.10}$$

where B_π is the velocity of the pion.

Figure IV-3 shows a plot of the two components of $P(\alpha,\beta)$ at the pion scattering angle $\alpha = 54.2$ deg. No muons are emitted beyond the

Table IV-VI. Results of the pion-decay correction.

θ_{LAB} (deg)	Counter geometry	f_μ^{OUT} (%)	f_μ^{IN} (%)	f_μ^{NET} (%)
11.0	LA	14.52	13.50	+1.02
14.8		14.60	13.54	+1.06
22.3		14.83	13.63	+1.20
22.3	SA	5.56	5.56	0.0
37.7		5.85	5.85	0.0
54.2		6.31	6.31	0.0
72.2		6.94	6.94	0.0
92.1		7.72	7.72	0.0
114.4		8.59	8.59	0.0
126.5		9.03	9.03	0.0
152.5		9.72	9.72	0.0

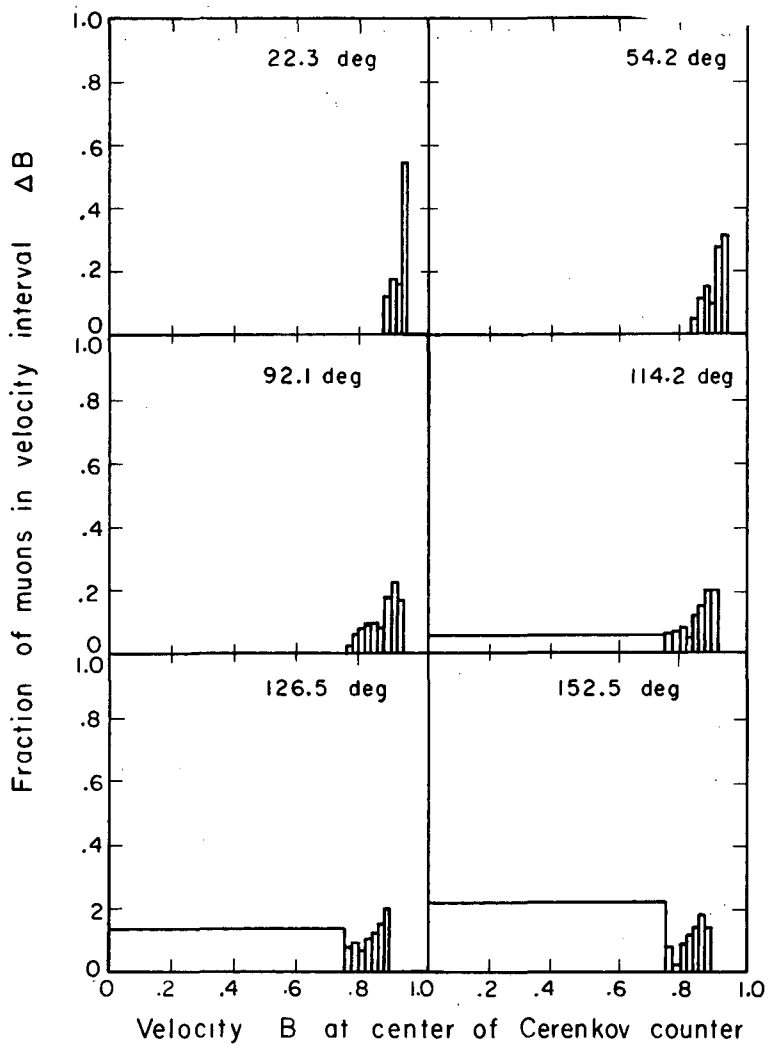

IV-5. Velocity distribution of muons from pion decay that count in S_1 and S_2.

lab angle β_{MAX} , which varied between 6.5 deg and 11.5 deg, depending on the pion scattering angle.

The variables used in the calculation of the multiple integral are shown in Fig. IV-4 in relation to the counter telescope. The integration over β in Eq. (4.7) extends over the solid angle subtended by the counter S_2 at the decay point. The dashed lines indicate limits imposed on ℓ by the requirement of a coincidence in the counters S_1 and S_2 . For a given telescope angle θ , the range of α is limited by the small magnitude of β_{MAX} , which also explains the reason why the variation of the pion differential cross section was neglected in Eq. (4.7).

The results of the calculations are given in Table IV-VI. For the SA counter geometry the correction is zero, because of the following argument. Neglecting for the moment the nonisotropic angular distribution of the pions and the presence of the counter S_1 , conservation of probability requires that as many pions decay before reaching S_2 as there are muons which enter this counter. Thus so far the correction vanishes. It remains to be shown that if S_1 is present all conceivable paths for a pion followed by its final-state muon lead through S_1 . The extreme test case results when one examines the pion that decays at the tip of S_1 . Can it reach the tip of S_2 ? The answer for the SA case is no, because of the small opening angle β_{MAX} . Only a nonlinear variation of the pion angular distribution could modify the above conclusion, but again the range of contributing pion scattering angles was small.

Nonetheless, f_μ^{IN} was also calculated for the SA counter geometry, in order to obtain a velocity distribution of these muons. Figure IV-5

shows this distribution at six selected pion telescope angles.

C. Cerenkov-Efficiency Corrections

The doubles rate for mesons $(S_1S_2)_M$ is defined in terms of the measured coincidence rate $(S_1S_2C)_{NET}$ as follows:

$$(S_1S_2)_M = \frac{(S_1S_2C)_{NET}\ (1-f_p)}{\epsilon} \quad . \tag{4.11}$$

The fraction of protons counted by the Cerenkov is f_p . The details of this correction are described in the second paragraph of this section. The generalized efficiency of the Cerenkov for all mesons is ϵ . Its details are given immediately below.

1. Efficiency for All Mesons

The basic difference between the measured efficiency ϵ_π and the desired efficiency ϵ derives from the presence of the counter S_3 in the logical expressions which make up the ratio ϵ_π ,

$$\left.\begin{aligned} \epsilon_\pi &= \frac{(S_1S_2S_3S_4S_5C)_{NET}}{(S_1S_2S_3S_4S_5)_{NET}} && \text{for } \theta_{LAB} \leqslant 90 \text{ deg} \\ &= \frac{(S_1S_2S_3C)_{NET}}{(S_1S_2S_3)_{NET}} && \text{for } \theta_{LAB} > 90 \text{ deg} \end{aligned}\right\} \tag{4.12}$$

Depending on the pion energy, 14% to 22% of the pions present in the center of S_2 scattered somewhere in the Cerenkov before reaching S_3 . If they scattered in the first few cm of water, their efficiency was considerably lower than the efficiency for pions, which continued to S_3 without a collision.

Therefore, it was necessary

(a) to distinguish between efficiencies for interacting and noninter-

acting mesons,

(b) to relate both of them to the measured efficiency for pions ϵ_π . Furthermore, both efficiencies had to be known as a function of velocity, because muons and scattered-in pions had different velocity distributions than pions scattered only in hydrogen.

To simplify matters in (b), ϵ_π was assumed as the efficiency for noninteracting pions, which scattered only once in the hydrogen target, or the efficiency for monoenergetic pions traversing the full 2-1/4 in. of water. This was a fairly good assumption in view of the 10 in. separation between C and S_3 , although some pions which interacted early with complex nuclei in C could have reached S_3 by means of final-state protons. The velocity of the hydrogen-scattered pion in the middle of C was assigned to this efficiency.

Before the efficiency for noninteracting mesons could be used to calculate the efficiency for interacting mesons, the former had to be known also as a function of the traversed distance in water. A mathematical expression could be obtained for this efficiency on the basis of Poisson statistics, provided one knew the mean number of photoelectrons at the first dynode of the photomultiplier and the photoelectron threshold of the Cerenkov channel. A simple calculation based on the gain of the photomultiplier and the known threshold of the first discriminator stage indicated a one-photoelectron threshold. To check on this finding, a least-square fit was made to the inefficiency data $(1-\epsilon_\pi)$ with expressions for this quantity based on one-, two-, three-, four-, and five-photoelectron thresholds. For a single-photoelectron threshold the formula for the

Table IV-VII. The measured Cerenkov efficiency ϵ_{π} as a function of the pion scattering angle.

θ_{LAB} (deg)	ϵ_{π} (%)
0.	99.90±0.20
45.8	98.60±0.60
54.2	98.10±0.40
72.2	98.30±0.30
90.0	97.00±0.30
92.1	95.26±0.54
114.4	92.75±0.83
126.5	89.68±0.76
152.5	79.13±0.68

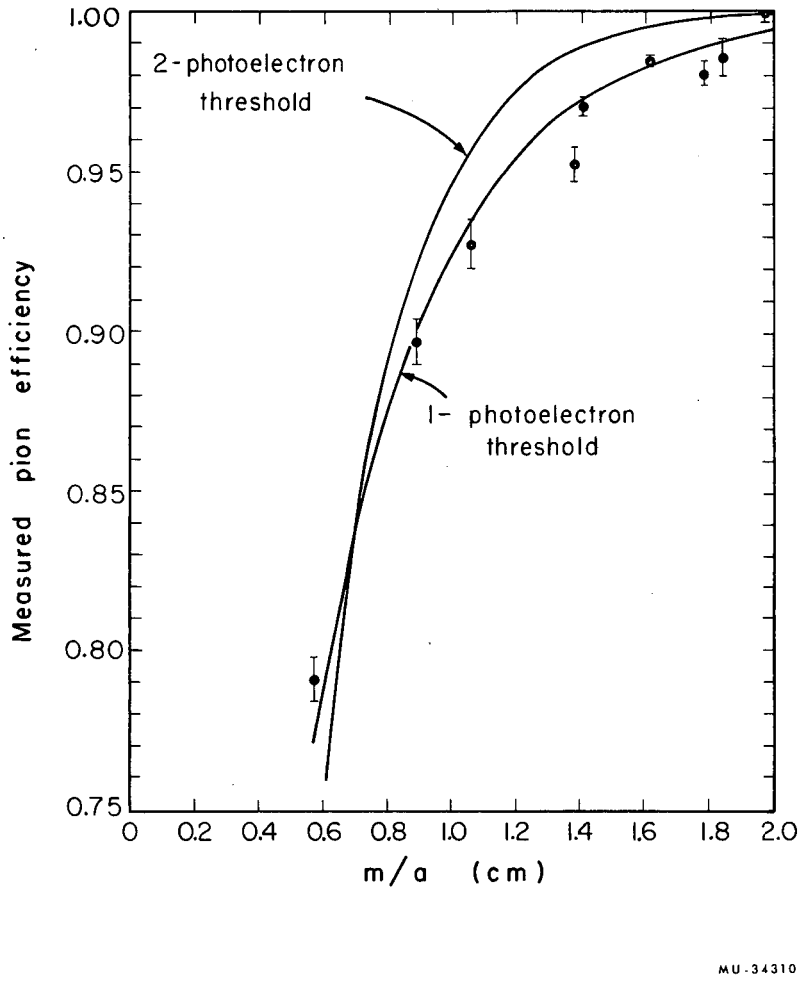

IV-6. Least-squares fits to the measured Cerenkov efficiencies for pions on the hypothesis of a one- and 2-photoelectron threshold in the Cerenkov channel.

inefficiency η_π is particularily simple,

$$\eta_\pi = (1-\epsilon_\pi) = \exp\left[-m\right] , \tag{4.13}$$

where the exponent m is the mean number of photoelectrons at the first dynode. This number is proportional to the intensity of the generated Cerenkov light and the distance covered by the pion in water (5.7 cm),

$$m = a(1 - \frac{1}{n^2B^2})5.7 , \tag{4.14}$$

where a is the parameter of the least-square fit in cm^{-1} , n is the index for water, and B is the velocity of the pion in the middle of the Cerenkov counter.

The one-photoelectron hypothesis gave by far the best fit to the inefficiency data. Dropping subcripts, substituting the best-fit parameter $a = 2.59 \pm 0.05\ cm^{-1}$ in Eq. (4.14), and using Eq. (4.13) yields the inefficiency for noninteracting mesons as a function of velocity and distance $x(cm)$ in water,

$$\eta(B,x) = \exp\left[-2.59(1- \frac{1}{n^2B^2})x\right] . \tag{4.15}$$

Table IV-VII gives a list of the measured efficiency ϵ_π as a function of the pion scattering angle. Figure IV-6 presents a plot of these data against m/a . Superimposed are the best fits based on one- and two-photoelectron thresholds.

Since attenuation in the Cerenkov must be considered, it will be more convenient from here on to refer to fractions of interacting or noninteracting mesons missed by the Cerenkov counter rather than to the corresponding inefficiencies.

Appendix A gives the detailed derivation of the overall Cerenkov efficiency ϵ . The general procedure for the calculation of ϵ was the following. Mesons in a given velocity bin ΔB at the center of S_2 were divided into interacting and noninteracting categories. All muons were in the second category, because they have no strong interactions with nuclei. For reasons of simplicity, scattered-in pions from the target walls and the counter S_1 were lumped with the monoenergetic pions, which scattered only once in hydrogen.

In order to obtain the fraction of mesons r which were noninteracting and which also were not counted in the Cerenkov counter, one would simply write

$$r(B) = t(B)\eta(B,5.7) \quad , \tag{4.16}$$

where $t(B)$ is the nuclear transmission coefficient for the velocity bin ΔB , and η is given by Eq. (4.15) evaluated at an average velocity along the 5.7-cm path in water.

The fraction of mesons r^* which interacted in the Cerenkov counter and which were not counted in the Cerenkov is a complicated expression involving the distance x to the point of interaction and the velocity of the incident pion B . One could write for this fraction, in a simplified form,

$$r^*(B) = \int t(B,x)\eta(B,x)\int P_{SCAT}(B,x,B',\alpha)\eta(B',\ell_\alpha)d\Omega_\alpha dx \ . \tag{4.17}$$

Here $\eta(B,x)$ is the pion inefficiency up to the scattering point x ; $t(B,x)$ is the corresponding nuclear transmission factor; $P_{SCAT}(B,B',x,\alpha)$ is the scattering probability $(sr^{-1}cm^{-1})$ at x and the scattering

angle α ; $\eta(B',\ell_\alpha)$ is the inefficiency for the final-state particle with velocity B' over its path ℓ_α from x to the water boundary.

The expression for $r^*(B)$ is made somewhat simpler than it would be in a general case by the fact that the function $\eta(B,x)$ is -- in this case, where one photoelectron is sufficient to give a count -- a simple exponential which factors easily into one factor attributable to the particle before scattering and a second factor for the particle after scattering.

Again, as in Section A, the inelastic scattering processes were divided into absorption and quasi-elastic events. The inefficiency $\eta(B,\ell_\alpha)$ for the first group was assumed to be 1, because final-state protons were below the Cerenkov threshold and second-order processes were neglected. Of course, in this case P_{SCAT} became the total probability for absorption (cm^{-1}) . The experimental data referred to in Section A2 were used for the scattering probabilities as well as for the velocity distributions of the quasi-elastic pions.

The results of the calculation of ϵ are given in Table IV-VIII. The origin of the assigned errors is as follows. First, since the Cerenkov-counter efficiency ϵ is the actual efficiency of the counter for all mesons (fast and slow, pions and muons) it is necessary to take account of any uncertainties in the composition of these particles in estimating the expected error in ϵ . Furthermore, each input parameter in the computation of r and r^* was varied in accordance with its expected uncertainty. The resultant changes in ϵ were then combined in quadrature.

Table IV-VIII. The overall Cerenkov efficiency ϵ.

θ_{LAB} (deg)	Counter geometry	ϵ (%)
11.0	LA	97.35±0.07
14.8		97.31±0.08
22.3		97.19±0.08
22.3	SA	97.02±0.08
37.7		96.54±0.10
54.2		95.60±0.11
72.2		93.85±0.14
92.1		91.69±0.24
114.4		87.78±0.34
126.5		84.23±0.43
152.5		72.39±0.72

Table IV-IX. Fraction of protons counted by the Cerenkov.

θ_{LAB} (deg)	Counter geometry	f_p (%)
11.0	LA	1.97±0.18
14.8		1.98±0.12
22.3		1.84±0.07
22.3	SA	1.84±0.07
37.7		0.76±0.29

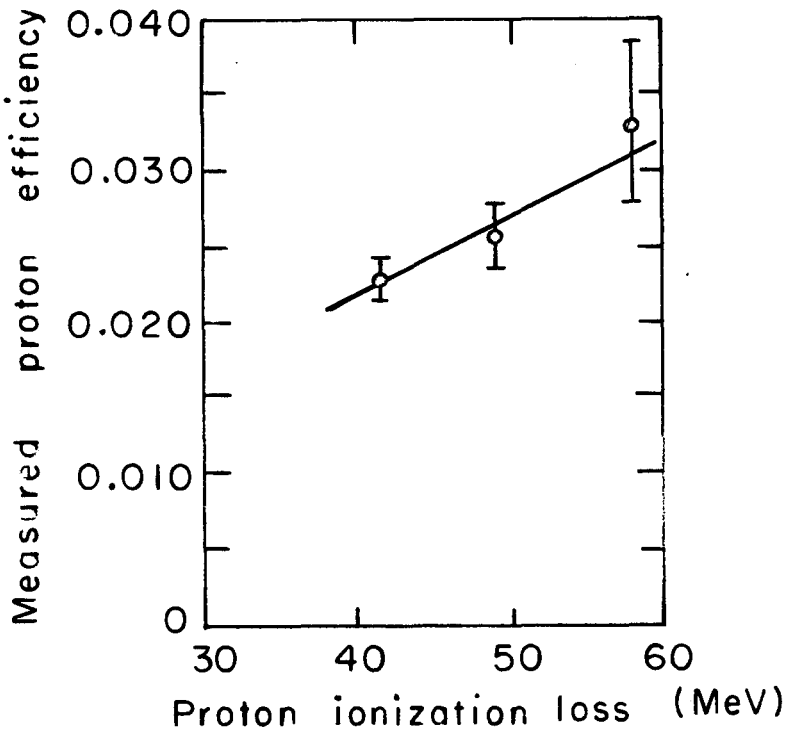

MU-34306

IV-7. Straight-line fit to the measured Cerenkov efficiencies for protons plotted against the ionization loss of the protons in the water of the Cerenkov counter.

2. Fraction of Protons Counted by the Cerenkov

The efficiency of the Cerenkov counter for protons ϵ_p was small. Figure IV-7 presents a plot of ϵ_p versus total ionization loss of the protons in the Cerenkov. If the positive slope of the fitted straight line is significant, it indicates scintillation in water as the probable mechanism responsible for the nonzero efficiency. The fraction of the total counts in $(S_1S_2C)_{NET}$ that are due to protons is given by

$$f_p = \frac{N_p \epsilon_p}{(S_1S_2)_{NET}} , \tag{4.18}$$

where N_p is the number of protons per ion volt present in the defining counter S_2. This quantity was deduced as follows:

$$N_p = \left[(S_1S_2S_3)_{NET} - \frac{(S_1S_2S_3C)_{NET}}{\epsilon_\pi} \right] \frac{(S_1S_2S_4S_5)_{NET}^{PROTONS}}{(S_1S_2S_3S_4S_5)_{NET}^{PROTONS}} . \tag{4.19}$$

The first factor represents the number of protons in S_3; the counting rates $(S_1S_2S_3)_{NET}$ and $(S_1S_2S_3C)_{NET}$ were part of the data collected at each scattering angle. The second factor gives the reciprocal attenuation of the Cerenkov counter for protons; it was measured together with the proton efficiency.

Values for f_p are given in Table IV-IX. No values are quoted beyond 37.7 deg in the laboratory system, since this is the angle at which protons stop in the Cerenkov counter.

D. Geometrical Correction

This correction results from the finite size of both the hydrogen target and the defining counter S_2. Combinations of different parts

Table IV-X. Geometrical correction.

θ_{LAB} (deg)	Counter geometry	g
11.0	LA	0.998
14.8		0.998
22.3		0.999
22.3	SA	0.994
37.7		0.996
54.2		1.000
72.2		1.003
92.1		1.000
114.4		0.997
126.5		0.997
152.5		0.997

of the target and the detector correspond to different scattering angles. Therefore, the contribution to the total scattering probability from each combination must be weighted by the appropriate differential cross section. Another source of variation in the scattering angle is the uncertainty in the incident beam direction. Assuming this uncertainty to be constant for all parts of the target, one can write, for the geometrical correction at the counter telescope angle θ_0, the equation

$$g(\theta_0) = \frac{1}{V\sigma(\theta_0)\Delta\Omega}\int P(|\theta-\theta_0|)\int_V\int_A \sigma(\alpha)\,\frac{\hat{r}\cdot\vec{dA}}{r^2}\,d\tau d\theta\ , \qquad (4.20)$$

where $d\tau$ is an element of the target volume V, dA is an element of the counter area A, $\hat{r}$ is a unit vector along the direction from dA to $d\tau$, and r is the distance between dA and $d\tau$; $P(|\theta-\theta_0|)$ is the probability per unit angle of a deviation $|\theta-\theta_0|$, measured in the scattering plane, from the principal incident beam direction; α is the scattering angle which corresponds to the modified counter telescope angle θ.

In order to simplify the evaluation of the multiple integral, the target was divided into 0.5-in. cubes and the counter S_2 into 0.5-in. squares. A Gaussian distribution was assumed for $P(|\theta-\theta_0|)$ with a measured half width of 2.0 deg at the half-maximum point. The differential cross sections $\sigma(\theta_0)$ and $\sigma(\alpha)$ were again obtained from existing experimental data.[10]

Results of the calculation are presented in Table IV-X.

E. Normalization and Results

The normalization of the corrected data to mb/sr was obtained in

Table IV-XI. Fitting parameters in the one-level resonance formula for the total π^+-p cross section.

Reference	Resonance energy E_o(MeV)	Reduced width γ_λ^2(MeV)	Channel radius $a(\frac{\hbar}{m_\pi c})$
This expmt.	160.2	63.8	0.895
Gell-Mann, Watson[28]	159	58	0.88

Table IV-XII. Total cross section data in the neighborhood of the 247.5-MeV incident-meson kinetic energy of this experiment.

Kinetic energy (MeV)	Total cross section (mb)	Reference no.
200 ± 5	177.9 ± 3.7	29
214 ± 8	141 ± 7	30
222 ± 8	148 ± 7	30
240 ± 6	125.6 ± 2.5	29
262 ± 9	111 ± 7	30
263 ± 9	107 ± 7	30
270 ± 6	85.2 ± 3.0	29

the following way.

In the first step, the one-level resonance formula by Brueckner[26] was fitted to a set of 50 experimental total cross-section values, with the help of a computer program written by Lach.[27] With the notation of Gell-Mann and Watson[28], the following expression results for the quantum numbers $T = \frac{3}{2}$, $J = \frac{3}{2}$, and $L = 1$ of the (3,3) resonance

$$\sigma_{TOT} = \frac{2\pi\hbar^2}{q^2} \frac{\Gamma^2}{(E-E_0)^2 + \frac{\Gamma^2}{4}} , \tag{4.21}$$

where the resonance width Γ is given by

$$\Gamma = \left[\frac{2\left(\frac{qa}{\hbar}\right)^3}{1+\left(\frac{qa}{\hbar}\right)^2} \right] \gamma_\lambda^2 . \tag{4.22}$$

Here q is the momentum in units of $m_\pi c$, E is the sum of the pion and nucleon kinetic energies, and E_0 is the kinetic energy of the resonance. All quantities are measured in the barycentric system. The channel radius is a, in units of $\hbar/m_\pi c$, and the reduced width is γ_λ^2. The last two quantities and E_0 were the fitting parameters. Table IV-XI gives a comparison between the best-fit parameters a, γ_λ^2, E_0 used in this experiment and those quoted by Gell-Mann and Watson. Applying the best-fit parameters to Eq. (4.22) and Eq. (4.21), one calculates

$$\sigma_{TOT} = 114.5 \pm 2.9 \text{ mb} \tag{4.23}$$

at 247.5 MeV incident-pion kinetic energy. Some total cross section data near 247.5 MeV are listed in Table IV-XII.

The data closest to the energy of the present experiment were those of Mukhin et al.[29] at 240 MeV. From the comments in their paper we deduced that we could take the value of the total cross section measured with a c.m. meson cutoff angle θ_c^* of 11 deg (and a corresponding cutoff angle $\theta_c^{*'}$ for the protons) to be 5 ± 1.5 mb less than the value quoted by Mukhin et al. for 0 deg cutoff angle. We therefore adopted as the total cross section at 247.5 MeV with 11 deg c.m. meson cutoff angle a value 5 ± 1.5 mb less than that given in expression (4.23). We used, then,

$$\sigma_{TOT} = 109.5 \pm 3.3 \text{ mb} \tag{4.24}$$

for 11 deg cutoff angle and incident-meson kinetic energy of 247.5 MeV. The corrected angular distribution and the phase-shift analysis were normalized to this value. The relative error above is 3%, which is also the uncertainty assigned to the absolute scale of the differential cross section.

A summary of the experimental data with its corrections is given in Table IV-XIII. The differential cross section is presented in Table IV-XIV as a function of the center-of-mass scattering angle θ^*; a plot of the same data is shown in Fig. IV-8.

F. Errors

The basic component of the errors assigned to the differential cross section in Table IV-XIV derives from counting statistics. This error was determined for a particular data point from the usual formula based on the Poisson distribution of the scattering events:

Table IV-XIII. Summary of the raw data, the applied corrections, and the corrected data.

θ_{LAB} (deg.)	Counter geometry	Raw Data $(S_1S_2C)_{NET}$ (counts/I.V.)	Fraction of counts due to protons fp (%)	Overall Cerenkov efficiency, ϵ (%)	Doubles rate $(S_1S_2)_M$ (counts/I.V.)	Net fraction of pions lost by scattering and decay, f (%)	Geometrical correction, g	Corrected data $\frac{(S_1S_2C)_{NET}(1-f_p)}{(1-f)\,\epsilon\, g}$ (counts/I.V.)
11.0	LA	1999.8±89.4	1.97±0.18	97.35±0.07	2013.8±92.0	+4.06±0.08	0.998	2103.2±96.1
14.8	LA	1755.3±47.6	1.98±0.12	97.31±0.08	1768.2±49.0	+4.11±0.08	0.998	1847.6±51.2
22.3	LA	1410.0±31.2	1.84±0.09	97.19±0.08	1424.0±32.0	+4.28±0.08	0.999	1489.8±33.5
22.3[a]	LA	1511.7±75.7	1.77±0.18	97.22±0.08	1527.4±77.9	+2.96±0.08	0.999	1576.2±80.4
22.3	SA	1454.8±13.8	1.84±0.07	97.02±0.08	1471.9±14.3	+2.83±0.08	0.994	1524.1±14.7
37.7	SA	866.2± 5.2	0.76±0.29	96.54±0.10	890.4± 6.1	+2.69±0.09	0.996	918.3± 6.3
54.2	SA	407.0± 4.8		95.60±0.11	425.7± 5.0	+2.83±0.11	1.000	438.2± 5.2
72.2	SA	176.4± 2.8		93.85±0.14	188.0± 3.0	+0.77±0.20	1.003	188.8± 3.0
90.0[b]	SA				154.3± 2.7	-0.52±0.37	1.000	153.5± 2.7
92.1	SA	137.4± 1.8		91.69±0.24	149.9± 2.0	-0.52±0.37	1.000	149.1± 2.1
114.4	SA	182.7± 3.6		87.78±0.34	209.6± 3.2	-0.24±0.27	0.997	209.7± 3.2
126.5	SA	198.7± 3.9		84.23±0.43	235.4± 4.6	+0.03±0.24	0.997	236.2± 4.6
139.2[b]	SA				265.1±13.7	-0.30±0.22	0.997	265.1±13.7
149.8[b]	SA				271.0± 5.1	-0.56±0.20	0.997	270.3± 5.1
152.5	SA	205.0± 3.9		72.39±0.72	283.2± 6.1	-0.64±0.20	0.997	282.2± 6.1

(a) These data were taken with a separation of 20.25 in. between S_1 and S_2.

(b) The doubles rate $(S_1S_2)_M$ was measured directly at these angles and at 114.4 deg., 126.5 deg. In the last two cases it was combined with the data derived from $(S_1S_2C)_{NET}$.

Table IV-XIV. Experimental π^+-p differential cross section in the center-of-mass system.[a]

θ^* (deg)	$\frac{d\sigma}{d\Omega^*}$ (mb/sr)	Relative error (%)
14.9	27.52 ± 1.26	4.6
20.0	24.46 ± 0.68	2.8
30.0	20.80 ± 0.18	0.9
49.9	13.927± 0.095	0.7
69.9	7.730± 0.093	1.2
89.9	3.930± 0.062	1.6
107.9	3.995± 0.069	1.7
109.9	3.969± 0.054	1.4
130.0	6.986± 0.107	1.5
140.0	8.73 ± 0.17	1.9
150.0	10.71 ± 0.55	5.1
158.0	11.57 ± 0.22	1.9
160.0	12.23 ± 0.26	2.1

[a]There is a 3% uncertainty in the absolute scale of the differential cross section.

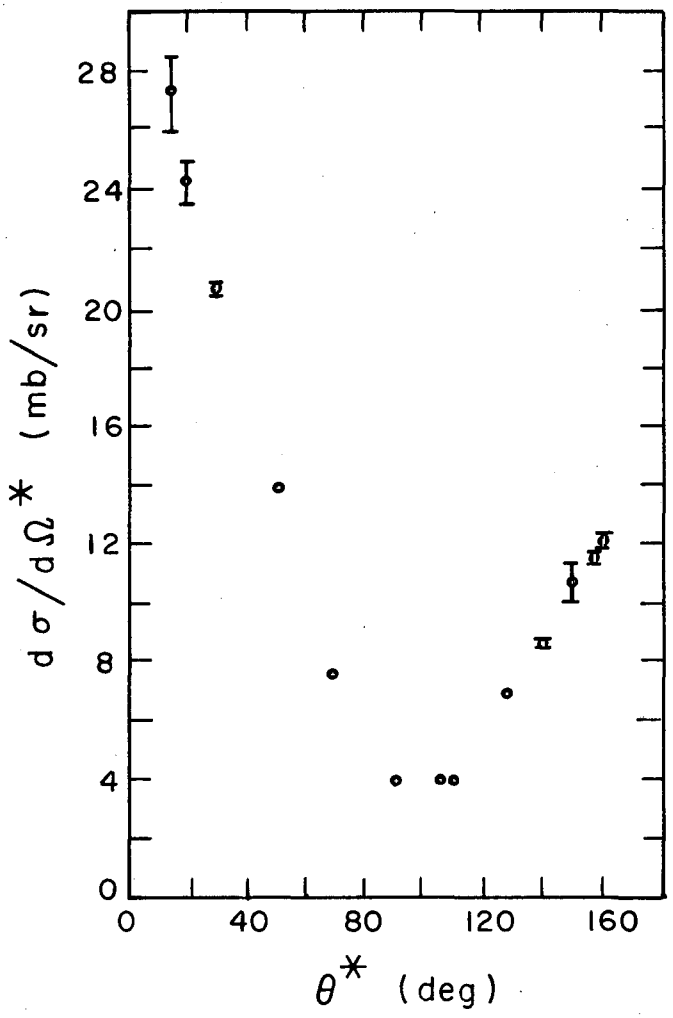

MU-34307

IV-8. Experimental differential cross section in the center of mass plotted against the center-of-mass scattering angle θ^*. (There is a 3% uncertainty in the absolute scale of the differential cross section).

$$\Delta\left(\frac{I(\theta)}{I_o}\right) = \left[\frac{I(\theta)}{I_o^{\,2}}\Big|_{FULL} + \frac{I(\theta)}{I_o^{\,2}}\Big|_{EMPTY}\right]^{1/2} \tag{4.25}$$

where I_o is the number of ion volts in a given beam exposure and $I(\theta)$ is the corresponding number of pions scattered into the solid angle of the counter telescope.

In the first step of the program for data correction a check was made on the adequacy of the error assignment based on Eq. (4.25). A consistency plot was prepared for the large number of data points at the 37.7 deg check angle. As mentioned in Chapter III.B, no significant trend with time was found in the data, but individual points were scattered about the average more than the standard deviations based on Eq. (4.25) would justify. This lack of repeatability very likely originated in background fluctuations and small shifts in position of the incident beam. A measure of the scattering effect was given by [31]

$$\sigma_{ext} = \sqrt{\frac{\chi^2}{d.f.}} \quad , \tag{4.26}$$

where χ^2 stands for the usual sum of squares of the error-weighted residuals,

$$\chi^2 = \sum_i \left[\frac{(X_i - \bar{X})}{\Delta X_i}\right]^2 \tag{4.27}$$

and d.f. is the number of degrees of freedom. For the sake of convenience X_i was written for the net hydrogen scattering rate at the ith data point, ΔX_i is given by Eq. (4.25), and $\bar{X}$ is the mean of the observations X_i .

Treating the standard deviation of Eq. (4.25) as an estimate of the true error at the data point i, the standard deviation of the mean $\bar{X}$ was written[32]

$$\Delta\bar{X} = \sigma_{ext} \sqrt{\frac{1}{\sum_i \frac{1}{\Delta X_i^2}}} , \qquad (4.28)$$

where $\sigma_{ext} = 1.57$ ($\theta_{LAB} = 37.7$ deg) was used at all laboratory-system angles. In other words, instead of computing the statistical counting errors from the usual expression (4.25) we have multiplied that expression by 1.57.

Considering the relatively high counting rates of this experiment, small counting errors, typically 1%, were the rule at practically all scattering angles. Therefore, systematic errors became very important. The preceding sections of this chapter are supposed to indicate a measure of the effort which was spent to calculate these errors and to obtain a realistic assessment of the uncertainties involved in their calculation. The errors assigned to the differential cross section include the estimated errors in all corrections.

Most of the corrections were small, which minimized the effect of their uncertainties. The exception to this rule was the overall Cerenkov efficiency ϵ. However, it is well to remember that the calculated part of this correction is roughly given by the difference $(\epsilon - \epsilon_\pi)$ between the overall Cerenkov-counter efficiency and the directly observed efficiency. This difference is about 2% for the forward angles and reaches 5.5% only for the backward angles. In the latter region comparison

is possible with the directly measured doubles rate (S_1S_2) , because recoil protons are absent here. The agreement between this rate and the bulk of the data derived from (S_1S_2C) was quite good. The (S_1S_2) data were therefore incorporated into the final results.

The agreement at the point of overlapping counter geometries $(\theta_{LAB} = 22.3 \text{ deg})$ was also satisfactory. This can be verified by reference to Table IV-12.

Table V-1. Polarization of the recoil proton for π^{+}-p scattering in the center-of-mass system.

θ (deg)	$P(\theta)$
68.0	0.290 ± 0.138
80.5	0.380 ± 0.126
108.4	0.219 ± 0.064
119.1	-0.035 ± 0.075
129.1	0.033 ± 0.068
138.0	-0.067 ± 0.062
147.0	-0.156 ± 0.072

V. PHASE-SHIFT ANALYSIS

Three distinct sets of data were used in the phase-shift analysis. In the first set were the 13 differential cross-section points given in Table IV-XIV. The second set consisted of the recoil-proton polarization measured at seven scattering angles by Schultz.[3] The mean incident-meson kinetic energy of that experiment was 246 MeV, which is within one standard deviation of the mean energy of the differential cross-section measurement. The polarization data are shown in Table V-1. Finally, there was the total cross-section at $\theta_c = 11$ deg given in Eq. (4.24).

Section A describes the relationship between the experimental data and the phase shifts; this section also shows the general features of the computer program which calculates the latter quantities. Section B presents the results of the analysis. A discussion of the results follows in Section C.

A. Search Program

1. Scattering Amplitudes

The connection between the differential cross section and the recoil-proton polarization on one hand, and the phase shifts on the other hand is usually expressed by means of the non-spin-flip scattering amplitude g and the spin-flip amplitude h.[33] The differential cross section for pions scattering from an unpolarized target is written

$$\frac{d\sigma}{d\Omega}(\theta) = |g(\theta)|^2 + |h(\theta)|^2 , \qquad (5.1)$$

where the star indicating a center-of-mass angle is omitted. All expressions in this chapter refer to the barycentric system only. The recoil-proton polarization is in turn written

$$\vec{P}(\theta) = \frac{2\mathrm{Re}\, g^*(\theta)h(\theta)}{|g(\theta)|^2+|h(\theta)|^2}\,\hat{n} = P(\theta)\hat{n}\ , \qquad (5.2)$$

where the unit vector $\hat{n}$ is defined in terms of the initial momentum $\vec{p}_i$ and the final momentum $\vec{p}_f$ by

$$\hat{n} = \frac{\vec{p}_i \times \vec{p}_f}{|\vec{p}_i \times \vec{p}_f|}\ .$$

Finally, neglecting Coulomb effects, the partial-wave expansions of the scattering amplitudes can be written

$$g(\theta) = \lambda\!\!\!^{-}\sum_{L=0}^{L_{MAX}}\left((L+1)\,\frac{\exp\left[2i\delta_L^{+}\right]-1}{2i} + L\,\frac{\exp\left[2i\delta_L^{-}\right]-1}{2i}\right)P_L(\cos\theta)\ , \qquad (5.3)$$

and

$$h(\theta) = \lambda\!\!\!^{-}\sum_{L=1}^{L_{MAX}}\left(\frac{\exp\left[2i\delta_L^{+}\right]-\exp\left[2i\delta_L^{-}\right]}{2}\right)P_L^{\,1}(\cos\theta)\ . \qquad (5.4)$$

Here, $\lambda\!\!\!^{-}$ is the wavelength divided by 2π ; L is the orbital angular-momentum quantum number; $P_L(\cos\theta)$ is the Legendre polynomial of order L ; $P_L^{\,1}(\cos\theta)$ is the associated Legendre polynomial of the same order, defined by

$$P_L^{\,1}(\cos\theta) = \sin\theta\,\frac{d}{d(\cos\theta)}\,P_L(\cos\theta)\ .$$

Finally, $\delta_L^{\pm}$ are the phase shifts for the orbital angular-momentum state L and the total angular momentum quantum number $J = L \pm 1/2$. The isotopic spin quantum number is suppressed in this notation; it is 3/2 for the π^+-p system. The phase shifts $\delta_L^{\pm}$ in Eqs. (5.3) and (5.4) are real quantities, since inelastic scattering has been neglected.

Expressions similar to Eqs. (5.3) and (5.4) which include Coulomb corrections are given in Appendix B.

It was pointed out in Chapter I that the differential cross section alone cannot determine the phase shifts uniquely. By inspection of Eq. (5.1) one will notice that the scattering amplitudes can be changed by arbitrary phase factors without affecting the magnitude of the differential cross section. This cannot be said of the expression for the polarization in Eq. (5.2). Hence its importance in a phase-shift analysis. Related to the rotations of g and h in the complex plane are transformations of the phase shifts from one set into another. The starting set is the Fermi set, characterized by a large positive δ_1^+ phase shift crossing 90 deg in the neighborhood of 190 MeV incident-pion kinetic energy.

The transformations which are often mentioned in the literature are listed below:

(a) Reversal of all phase-shift signs. This ambiguity can be resolved by the measurement of the differential cross section at forward pion scattering angles[34] where the interference with Coulomb phase shifts is appreciable.

(b) The Yang transformation[35], in which the sign of $(\delta_1^+ - \delta_1^-)$ is

reversed.

(c) A similar transformation[36] relating to the δ_2 phase shifts.

(d) The Minami transformation,[37] where all phase shifts of the same J and different L are interchanged.

It is the object of this phase-shift analysis to eliminate the above ambiguities through statistical tests.

2. Computing Method

The IBM 7090 program PIPANAL IV, developed by Foote,[38] was used in the analysis. The method of computation rests on the grid search method,[39] in which a set of input phase shifts is varied by a constant increment until a minimum of the quantity

$$\chi^2 = \sum_i \left[\frac{X_i^{(c)} - X_i^{(e)}}{\Delta X_i} \right]^2 \qquad (5.5)$$

is reached. Here, $X_i^{(e)}$ is the experimental value of the differential cross section, polarization or total cross section; ΔX_i is its experimental error. The corresponding quantity calculated by the program from Eqs. (B.1), (B.2), (5.1), and (5.2) for a given set of phase shifts is given by $X_i^{(c)}$; the summation over the index i extends over all data points. The above sequence completes one cycle. In the following cycles the initial phase-shift increment is steadily decreased, the program seeking each time the nimimum of the expression in Eq. (5.5). This procedure continues until the cycle for a preset smallest increment is completed. The corresponding minimum of χ^2 is the lowest for this particular set of input phase shifts. However, other initial sets may

Table V-II. Phase-shift solutions.

1. SPD phase-shift solution

Solution	Nuclear phase shifts					χ^2 (Expected: 15)		
	$S_{3,1}$	$P_{3,1}$	$P_{3,3}$	$D_{3,3}$	$D_{3,5}$	Total	DCS[a]	POL[a]
Fermi-I	-18.3±0.6	-7.3±0.6	118.9±1.3	0.9±0.6	-1.9±0.6	15.5	11.6	3.9

2. SPDF phase-shift solutions

Solution	Nuclear phase shifts							χ^2 (Expected: 13)		
	$S_{3,1}$	$P_{3,1}$	$P_{3,3}$	$D_{3,3}$	$D_{3,5}$	$F_{3,5}$	$F_{3,7}$	Total	DCS[a]	POL[a]
A	-18.4±0.7	-8.0±1.6	119.3±1.3	0.0±1.6	-1.3±1.3	0.0±0.8	0.6±1.0	13.3	8.9	4.4
B	-18.7	-12.2	153.2	2.3	-24.6	-4.1	21.0	20.1	13.1	7.0
C	-37.6	-13.9	146.5	-13.5	21.5	-0.7	-3.4	22.8	7.7	15.1

(a) These columns list the contributions to the total χ^2 from the differential cross section (DCS) and the recoil-proton polarization (POL).

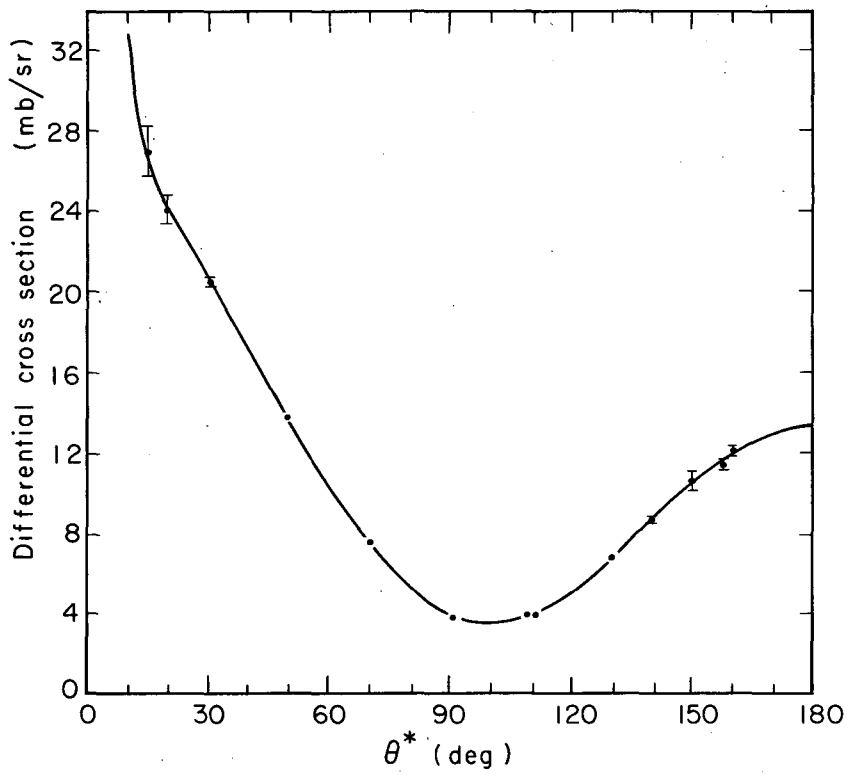

MU-34299

V-1. Fit to the experimental data of the differential cross section calculated from the phase shifts of the SPD Fermi-I solution.

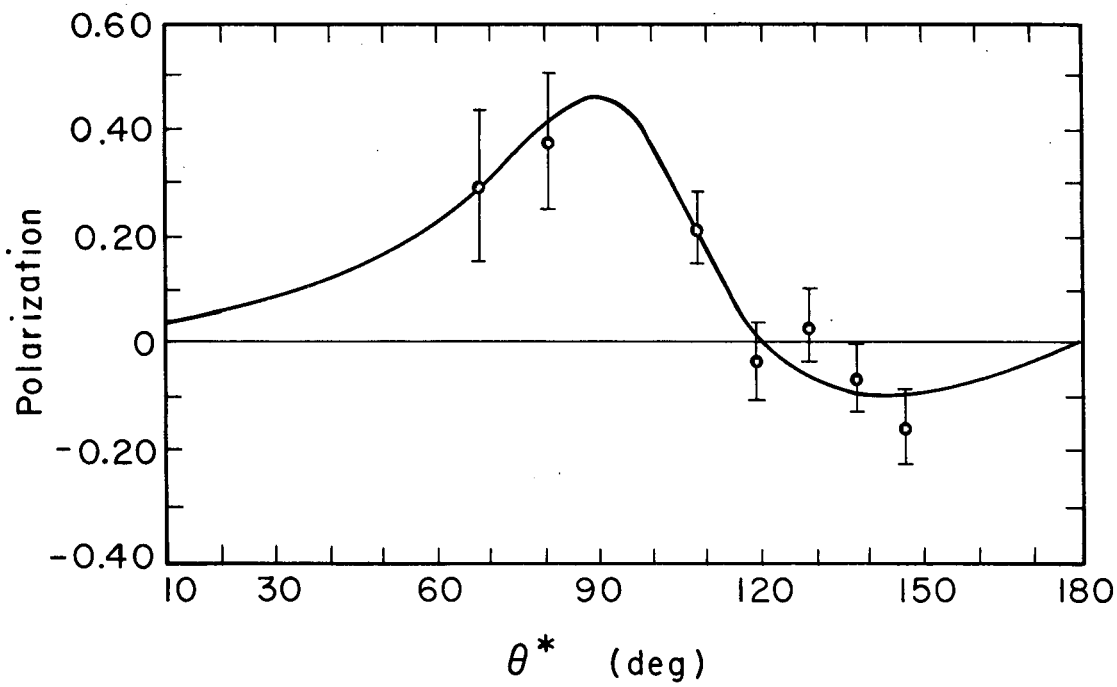

MU-34298

V-2. Fit to the experimental data of the recoil-proton polarization calculated from the phase shifts of the SPD Fermi-I solution.

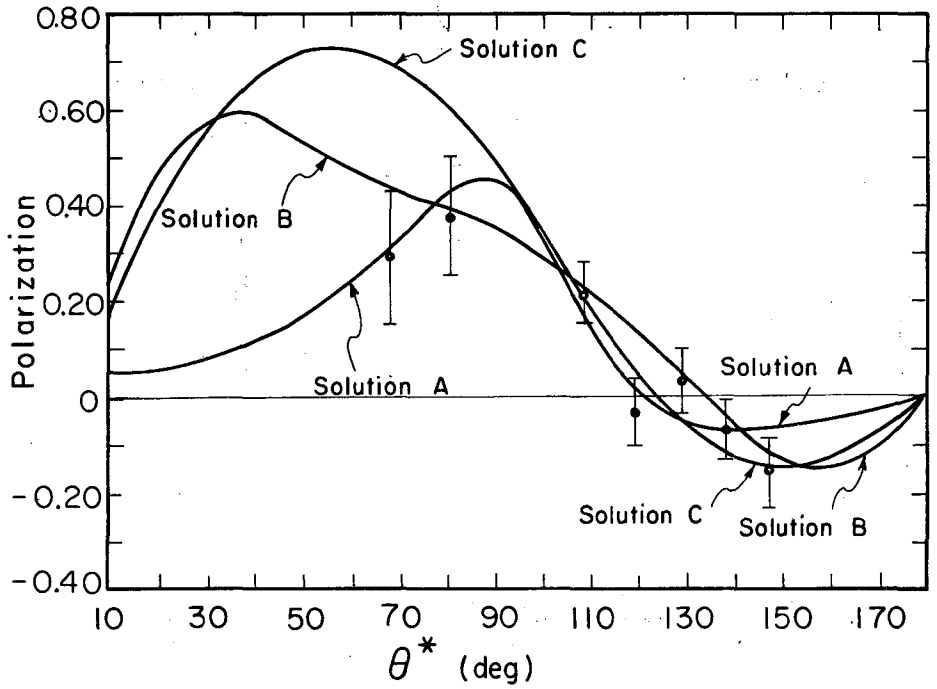

MU-34293

V-3. Recoil-proton polarization data and the corresponding values calculated from the three SPDF phase-shift solutions.

lead to different minima and lower χ^2 .

To establish the uncertainty in the set of phase shifts accompanying the minimum χ^2 , the program calculates the matrix elements

$$G_{ij} = \frac{\partial^2(\chi^2)}{\partial\delta_i \partial\delta_j} \quad , \tag{5.6}$$

where the inices i,j range over the number of phase shifts δ . The errors assigned to the phase shifts are obtained from the diagonal elements of the inverse matrix G^{-1} (error matrix):[40]

$$\Delta\delta_i = \sqrt{(G^{-1})_{ii}} \quad . \tag{5.7}$$

B. Results

1. SPD Analysis

The notation of spectroscopy, S,P,D,F, etc., is used in this section to denote the orbital angular momentum quantum number $L = o,1,2,3,$ etc. The subscripts $2T,2J$ will again indicate the isotopic spin and total angular momentum quantum numbers.

It was already apparent from the normalization of the differential cross section that D waves were necessary for an adequate fit. Thus, a SP analysis was omitted.

Three hundred different sets of random phase shifts, ranging from -90 deg to +90 deg, were fed into the computer together with the data listed at the beginning of this chapter. Only one set of phase shifts fitted the differential cross-section and polarization data well. This solution is listed in Table V-II-1 under the label Fermi-I (I means $D_{3,3}-D_{3,5} > 0$). Figures V-1 and V-2 show the experimental data and the corresponding values calculated from the Fermi-I phase-shift set. Other solutions representing the various ambiguities mentioned in Section A also appeared, but their likelihood of being the correct set was less than 1%.

2. SPDF Analysis

It was decided to include F waves despite their expected small magnitude, because of the often-demonstrated sensitivity of the polarization data to the small phase shifts.

This time, 240 initial sets of phase shifts were used as the starting points of the analysis. Again, these phase shifts were selected at

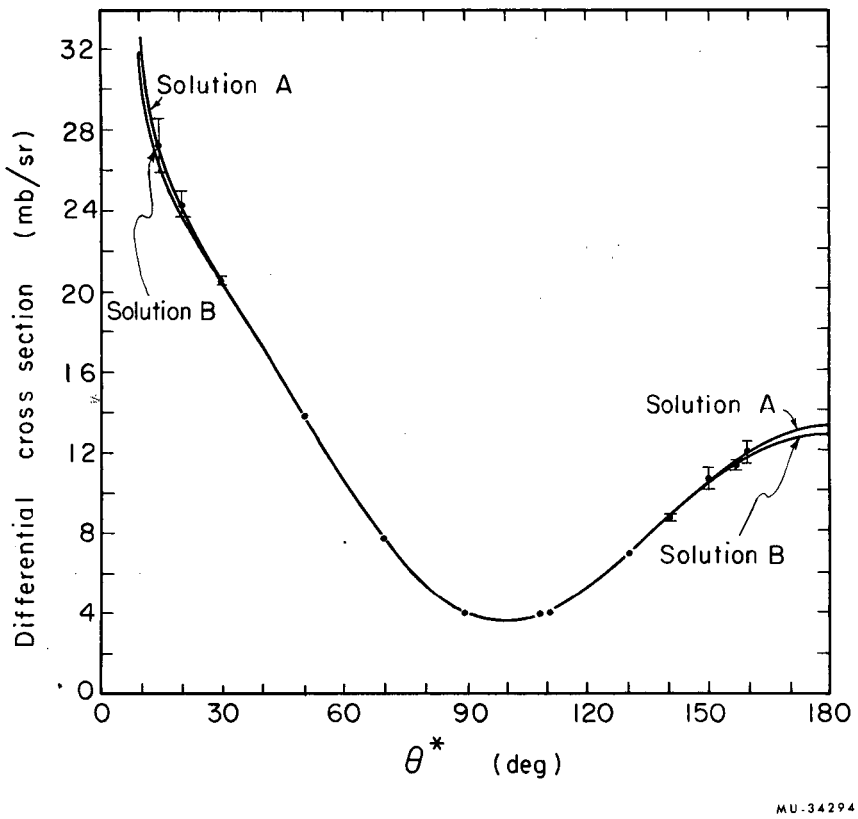

V-4. Comparison between the fits to the experimental data of the differential cross sections based on the phase shifts of SPDF solution A and solution B.

random with the exception of the F phase shifts, which were set to zero.

The results, which are shown in Table V-II-2, are similar to those of Foote.[38] Although the SPDF counterpart of the SPD Fermi-I solution was found (solution A), two other solutions also emerged that had low χ^2. Solution B is of the Fermi-I type. It has a very large $F_{3,7}$ phase shift, therefore, it can be neglected on this ground. Solution C is analogous to Foote's Fermi-II solution. On the basis of the χ^2 distribution alone it has less than a 5% chance of being the right solution. More convincing, perhaps, is the more than threefold increase in the χ^2 contribution from the polarization between solutions A and C. A qualitative argument can be made directly from the plot of the polarization data in Fig. V-3, where the calculated polarizations based on the three SPDF solutions are shown. While the backward angles are equally well fitted by either solution, the two measurements at 60.8 and 80.5 deg clearly favor solution A. The conclusion is, therefore, that solution A best fits the polarization and differential cross-section data.

C. Discussion

At first sight, the SPDF results may look alarming, as they did to Foote et al.[38], who first attempted to extend the analysis to include F waves. The proper interpretation of the emergence of several solutions is the exhaustion of the information contained in the majority of the experimental data, namely, the differential cross section. This point is illustrated in Fig. V-4, where the fits of solutions A and B are compared. (The fit of solution C is indistinguishable from that of

solution A). A large $D_{3,5}$ phase shift of -24.6 deg, coupled with a 21.0 deg $F_{3,7}$ phase shift, makes only a small difference at the extreme forward and backward angles, where the accurate measurement of the differential cross section is exceedingly difficult in any case. The large increase in the errors assigned to the small phase shifts of solution A is another manifestation of this loss of resolution. Nevertheless, the magnitude of these errors is somewhat deceiving because of the large amount of correlation that exists between the phase shifts. Consequently, the error matrices of the accrptable SPD and SPDF solutions are also given in Appendix C.

The agreement with other experiments, notably with Foote and Rogers, is good. The evidence which led to the rejection of solution C (Fermi-II) is substantiated by Vik and Rugge,[41] who performed a SPDF analysis at 310 MeV using data from π^--p elastic scattering, recoil-proton polarization, and charge-exchange scattering. These authors found no solution fitting all their data by starting the search from Foote's Fermi-II solution. Finally, the phenomenological analysis by Roper[42] predicts phase shifts at 247 MeV which are very close to those of solution A.

Comparison with theory is made only with the most recent work by Donnachie, Hamilton, and Lea,[43] which is based on dispersion relations for the partial-wave scattering amplitudes. Due to the method of their analysis, their predictions are valid only for $L \geq 1$, but they improve with increasing L. The results of these calculations are

$P_{3,1}$	$D_{3,3}$	$D_{3,5}$	$F_{3,5}$	$F_{3,7}$
-9.2 ± 0.8	-0.5 ± 0.2	-1.3 ± 0.1	-0.04 ± 0.04	0.34 ± 0.05

Solution A fits these predictions best.

Summarizing, while only one acceptable SPDF solution was found, no claim can be made that the polarization and differential cross-section data alone, no matter how accurately measured, are capable of establishing the small phase shifts accurately. A proposal[44] has been advanced to measure the spin rotation coefficients, since they are capable of sensitive discrimination against the Fermi-II solution. However, technical difficulties[3] will delay the measurement of these parameters for some time. Therefore, π^--p scattering that involves both the isotopic-spin $T = 3/2$ and $T = 1/2$ states will in the near future remain the only possible source of accurate phase-shift analyses in the pion-nucleon system.

ACKNOWLEDGMENTS

I should like to express my gratitude to Professor Owen Chamberlain for his scientific help and guidance throughout my graduate years. The help and advice of Dr. Gilbert Shapiro during the experiment and analysis is greatly appreciated. I have also benefited considerably from my association with Dr. Sinjiro Yasumi.

Permission to the compilation of differential cross sections by Dr. Joseph Lach is gratefully acknowledged.

Much hard work during the experiment was provided by Mr. Eric Arens, Mr. Fred Betz, Mr. Helmut Dost, and Dr. Claude Schultz.

I also wish to thank the cyclotron crew under Mr. James T. Vale and the personnel of the computer center under the supervision of Mr. Kent Curtis for their cooperation.

APPENDICES

A. Generalized Cerenkov Efficiency for All Mesons

Following is a derivation of the overall efficiency $\mathcal{E}$, which relates the doubles-rate for mesons $(S_1S_2)_M$ to the measured coincidence rate $(S_1S_2C)_{NET}$. According to the definition in Chapter IV.C,

$$(S_1S_2)_M = \frac{(S_1S_2C)_{NET}(1-f_p)}{\mathcal{E}} \quad , \tag{4.11}$$

where f_p is the fraction of protons counted by the Cerenkov.

Three different varieties of mesons were distinguished at the center of the defining counter S_2. First, there were the monoenergetic pions, which scattered once in hydrogen. Scattered-in pions from the target walls and the counter S_1 were lumped with them for reasons of simplicity. The remaining two groups of mesons consisted of double-scattered pions in hydrogen and muons from pion decay.

The velocity distribution of each meson variety was divided into bins $\Delta B = 0.02$ wide, except for the region $B < 0.75$, which was below the Cerenkov threshold. The mesons in each velocity bin were in turn divided into interacting and noninteracting categories. Treating each category separately, one can expand the right-hand side of Eq. (4.11) and write, at a given pion scattering angle,

$$\begin{aligned}(S_1S_2)_M = (S_1S_2C)_{NET}(1-f_p) + \frac{(S_1S_2)_M}{(1-f)}\Bigg[&\left(1-f_\pi^{H,OUT}-f_\mu^{OUT}-f_\pi^{W,NET}-f_\pi^{S,NET}\right)(r+r^*) \\ &+\sum_i f_\pi^{H,IN}(B_i)\left(r_H(B_i) + r_H^*(B_i)\right) + \sum_i f_\mu^{IN}(B_i)\eta(B_i,5.7)\Bigg] \quad ,\end{aligned} \tag{A.1}$$

where f is the fraction of pions lost by second nuclear scattering and pion decay, and $f_\pi^{H,NET}$, $f_\pi^{W,NET}$, $f_\pi^{S,NET}$, and f_μ^{NET} are its net contributions from the various second-order processes (Eq. 4.2); r and r^* (with or without subscripts)are the fractions of noninteracting and interacting mesons missed by the Cerenkov, given respectively by Eq. (4.16) and Eq. (4.17); η is the inefficiency for noninteracting mesons, as shown in Eq. (4.15).

Using Eq. (4.11) to eliminate $(S_1S_2)_M$ in Eq. (A.1), one obtains an expression for ϵ,

$$\epsilon = 1 - \left[\frac{(1-f_\pi^{H,OUT}-f_\mu^{OUT}-f_\pi^{W,NET}-f_\pi^{S,NET})(r+r^*)}{(1-f)} + \frac{\sum_i f_\pi^{H,IN}(B_i)\left(r_H(B_i) + r_H^*(B_i)\right) + \sum_i f_\mu^{IN}(B_i)\eta(B_i,5.7)}{(1-f)} \right] . \tag{A.2}$$

B. Coulomb-Corrected Scattering Amplitudes

The partial-wave expansions of the scattering amplitudes given by Eqs. (5.3) and (5.4) can be rewritten to include the effects of Coulomb scattering of the incident pion on the target proton. The relations given below, taken from Foote,[38] are correct relativistically to first order. The method of correction used is essentially that of Stapp, Ypsilantis, and Metropolis.[45]

$$g(\theta) = -\frac{\lambda\!\!\!^{-} n}{2\sin^2(\theta/2)} \exp\left[-in\,\ell n\left(\sin^2(\theta/2)\right)\right]$$

$$+ \lambda\!\!\!^{-} \sum_{L=0}^{L_{MAX}} \left((L+1) \frac{\exp\left[2i\,\delta_L^+\right] - \exp\left[2i\,\Phi_L\right]}{2i} \right.$$

$$\left. + L \frac{\exp\left[2i\,\delta_L^-\right] - \exp\left[2i\,\Phi_L\right]}{2i} \right) P_L(\cos\theta) \quad , \quad (B.1)$$

$$h(\theta) = \frac{i\lambda\!\!\!^{-} n\, B \sin\theta}{2\sin^2(\theta/2)} + \lambda\!\!\!^{-} \sum_{L=1}^{L_{MAX}} \left(\frac{\exp\left[2i\,\delta_L^+\right] - \exp\left[2i\,\delta_L^-\right]}{2} \right.$$

$$\left. - in\,B \frac{2L+1}{L(L+1)} \right) P_L^{\,1}(\cos\theta) \quad . \qquad (B.2)$$

All symbols in the above equations that are identical to those used in Eqs. (5.3) and (5.4) retain the same meaning, with the exception of the phase shifts: $\delta_L^{\pm}$ now stands for the <u>total</u> phase shift, defined by

$$\delta_L^{\pm} = \delta_{L,N}^{\pm} + \Phi_L + \Delta\Phi_L^{\pm} \quad , \qquad (B.3)$$

where $\delta_{L,N}^{\pm}$ is the nuclear phase shift. The nonrelativistic Coulomb phase shift is Φ_L , given by

$$\left.\begin{aligned} \Phi_o &= 0 \qquad\qquad , \text{ for } L = 0 \ , \\ \Phi_L &= \sum_{x=1}^{L} \tan^{-1}\left(\frac{n}{x}\right) , \text{ for } L \geqslant 1 \ , \end{aligned}\right\} \qquad (B.4)$$

where n , also used in Eqs. (B.1) and (B.2), is defined by

$$n = \frac{e^2}{\hbar v} ,$$

with v as the velocity of the incident pion in thelaboratory-system. The last term in Eq. (B.3) is the first-order relativistic correction to the nonrelativistic Coulomb phase shift Φ_L ,

$$\left.\begin{aligned} \Delta\Phi_o &= n\,\frac{(\beta_\pi\,\beta_p)/2 + (2\mu_p-1)\beta_p^{\,2}/4}{1+\beta_\pi\,\beta_p} &&, \text{for } L = 0 , \\ \Delta\Phi_L^+ &= \frac{nB}{L+1} &&, \text{for } L \geqslant 1 , \\ \Delta\Phi_L^- &= -\frac{nB}{L} &&, \text{for } L \geqslant 1 , \end{aligned}\right\} \qquad (B.5)$$

where β_π and β_p are the center-of-mass velocities of the pion and proton respectively in units of c,μ_p is the magnetic moment of the proton in nuclear magnetons, and B , also used in Eqs. (B.1) and (B.2), is defined by

$$B = \frac{(\mu_p\,\beta_\pi\,\beta_p)/2 + (2\mu_p-1)\beta_p^{\,2}/4}{1 + \beta_\pi\,\beta_p} .$$

The nonrelativistic Coulomb phase shifts for the incident-pion kinetic energy of 247.5 MeV and their relativistic corrections are presented in Table BI.

Table BI. Coulomb phase shifts (in deg) at the incident-pion kinetic energy of 247.5 MeV. $\Phi_L^{\pm} = \Phi_L + \Delta\Phi_L^{\pm}$ are the total Coulomb phase shifts.

L	Φ_L	$\Delta\Phi_L^+$	$\Delta\Phi_L^-$	Φ_L^+	Φ_L^-
0	0.00	0.07		0.07	
1	0.45	0.07	-0.15	0.52	0.30
2	0.67	0.05	-0.07	0.72	0.60
3	0.82	0.04	-0.05	0.86	0.77

Appendix C. Tables of Error Matrices for SPD and SPDF Solutions

Table C-I. Error matrix G^{-1} for the SPD Fermi-I solution (in deg^2).

	$S_{3,1}$	$P_{3,1}$	$P_{3,3}$	$D_{3,3}$	$D_{3,5}$
$S_{3,1}$	0.42	0.29	0.61	0.17	-0.17
$P_{3,1}$		0.37	0.43	0.16	-0.19
$P_{3,3}$			1.57	0.00	0.07
$D_{3,3}$				0.33	-0.26
$D_{3,5}$					0.32

Table C-II. Error matrix G-1 for the SPDF solution A (in deg^2).

	$S_{3,1}$	$P_{3,1}$	$P_{3,3}$	$D_{3,3}$	$D_{3,5}$	$F_{3,5}$	$F_{3,7}$
$S_{3,1}$	0.48	0.76	0.40	0.66	-0.54	0.26	-0.36
$P_{3,1}$		2.68	-0.38	+2.44	-1.97	1.11	-1.61
$P_{3,3}$			1.84	-0.71	0.68	-0.34	0.49
$D_{3,3}$				2.53	-1.99	1.05	-1.57
$D_{3,5}$					1.69	-0.84	1.22
$F_{3,5}$						0.57	-0.74
$F_{3,7}$							1.10

REFERENCES

1. James H. Foote, Owen Chamberlain, Ernest H. Rogers, Herbert M. Steiner, Clyde E. Wiegand, and Thomas Ypsilantis, Phys. Rev. 122, 948 (1961).

2. Ernest H. Rogers, Scattering of 310-MeV Positive Pions by Protons: Experiments and Analysis (Thesis) UCRL-10127, March 1962.

3. Claude H. Schultz, Scattering of 250-MeV Positive Pi Mesons from a Polarized Proton Target (Thesis), UCRL-11149, January 1964. (unpublished).

4. S. Mandelstam, Proc. Roy. Soc. (London) A244, 491 (1958).

5. R. A. Swanson, 0.5-BeV/c Beam Transport System, University of California at San Diego, preprint (unpublished).

6. O. Chamberlain, E. Segrè, and C. Wiegand, Phys. Rev. 83, 923 (1951).

7. K. Saito and K. Suga, Nuovo Cimento 11, 600 (1959).

8. Bob Acker, A Tunnel Diode Discriminator for Constant Delay Applications, UCID-1982, July 1963 (unpublished).

9. William Wenzel, Millimicrosecond Coincidence Circuit for High-Speed Counting, UCRL-8000, Oct. 1957 (unpublished).

10. Joseph Lach, Effects of the Single Pion Exchange in the Reaction $p + p \rightarrow n + p + \pi^+$ (Thesis)UCRL-10718, March 1963.

11. A. G. Meshkovskii and Ya. Ya. Shalamov, Soviet Phys.--JETP 10, 697 (1960).

12. M. Shafi and D. J. Prowse, The Interactions of 95-MeV π^+ Mesons with Emulsion Nuclei, from International Conference on Mesons and Recently Discovered Particles, (Padova-Venezia, 1957) X-2.

13. Wang Kan-Chang, Wang Tso-Tsiang, Ding Da-Tsao, L. N. Dubrovskii, E. N. Kladnitskaia, and M. I. Solov'ev, Soviet Phys.--JETP 8, 625 (1959).

14. G. E. Belovitskii, Soviet Phys.--JETP 8, (1959).

15. G. A. Blinov, M. F. Lomanov, Ya. Ya. Shalamov, V. A. Shebanov, and V. A. Shchegolev, Soviet Phys.--JETP 8, (1959).

16. G. Ferrari, L. Ferretti, R. Gessaroli, E. Manaresi, E. Pedretti, G. Puppi, G. Quareni, A. Ranzi, A. Stanghellini, and S. Stantic, Suppl. Nuovo Cimento 4, 914 (1956).

17. John O. Kessler and Leon M. Lederman, Phys. Rev. 94, 689 (1954).

18. B. A. Nikol'skii, L. P. Kudrin, and S. A. Aki'zade, Soviet Phys.--JETP 5, 93 (1957).

19. N. I. Petrov, V. G. Ivanov, and V. A. Rusakov, Soviet Phys.--JEPT 10, 682 (1960).

20. A. H. Morrish, Phil. Mag. 45, 47 (1954).

21. V. P. Dzhelepov, V. G. Ivanov, M. S. Kozodaev, V. T. Osipenkov, N. I. Petrov, and V. A. Rusakov, Soviet Phys.--JETP 4, 864 (1957).

22. W. F. Baker and J. Rainwater, Phys. Rev. 112, 1763 (1958).

23. Tadao A. Fujii, Phys. Rev. 113, 695 (1959).

24. S. Fernbach, R. Serber, and T. B. Taylor, Phys. Rev. 75, 1352 (1949).

25. R. M. Frank, J. L. Gammel, and K. M. Watson, Phys. Rev. 101, 891 (1956).

26. K. A. Brueckner, Phys. Rev. 86, 106 (1952).

27. Joseph Lach (Yale University), private communication.

28. M. Gell-Mann, and K. M. Watson, Ann. Rev. Nucl. Sci. 4, 219 (1954).

29. A. I. Mukhin, E. B. Ozerov, B. M. Pontecorvo, E. L. Grigoriev, and N. A. Nitin, Positive Pion-Proton Scattering at the Energies 176, 200, 270, 307, and 310 MeV, from Proceedings of the CERN Symposium on High-Energy Accelerators and Pion Physics, Vol. II (CERN, Geneva, 1956), p. 204.

30. S. J. Lindenbaum and L. C. L. Yuan, Phys. Rev. 100, 306 (1955).

31. W. E. Deming, Statistical Adjustment of Data (John Wiley and Sons, New York, 1948).

32. P. Cziffra and M. J. Moravscik, A Practical Guide to the Method of Least Squares, UCRL-8523, June 1958.

33. J. Ashkin, Nuovo Cimento Suppl. 14, Ser. X, No. 2, 221 (1959).

34. J. Orear, Phys. Rev. 96, 1417 (1954).

35. H. A. Bethe and F. de Hoffmann, Mesons and Fields (Row, Peterson, and Company, Evanston, Illinois, 1955), Vol. II, p. 72.

36. E. Clementel and C. Villi, Nuovo Cimento 5, 1343 (1957).

37. Shigeo Minami, Progr. Theoret. Phys. (Kyoto) 11, 213 (1954).

38. James H. Foote, Owen Chamberlain, Ernest H. Rogers, and Herbert M. Steiner, Phys. Rev. 122, 959 (1961).

39. E. Fermi, N. Metropolis, and E. F. Alei, Phys. Rev. 95, 1581 (1954).

40. H. L. Anderson, W. C. Davidon, M. Glicksman, and V. E. Kruse, Phys. Rev. 100, 279 (1955).

41. Hugo R. Rugge and Olav T. Vik, Phys. Rev. 129, 2300 (1963); Olav T. Vik and Hugo Rugge, Phys. Rev. 129, 2311 (1963).

42. L. David Roper, Phys. Rev. Letters 12, 340 (1964).

43. A. Donnachie, J. Hamilton, and A. T. Lea, Phys. Rev. 135, B515 (1964).

44. Young S. Kim, Phys. Rev. 129, 862 (1963).

45. H. P. Stapp, T. J. Ypsilantis, and N. Metropolis, Phys. Rev. 105, 302 (1957).

This report was prepared as an account of Government sponsored work. Neither the United States, nor the Commission, nor any person acting on behalf of the Commission:

A. Makes any warranty or representation, expressed or implied, with respect to the accuracy, completeness, or usefulness of the information contained in this report, or that the use of any information, apparatus, method, or process disclosed in this report may not infringe privately owned rights; or

B. Assumes any liabilities with respect to the use of, or for damages resulting from the use of any information, apparatus, method, or process disclosed in this report.

As used in the above, "person acting on behalf of the Commission" includes any employee or contractor of the Commission, or employee of such contractor, to the extent that such employee or contractor of the Commission, or employee of such contractor prepares, disseminates, or provides access to, any information pursuant to his employment or contract with the Commission, or his employment with such contractor.